APPLICATION OF SATELLITE-BASED SIDELOOKING RADAR IN MARITIME SURVEILLANCE

BY

EINAR-ARNE HERLAND

DTIC
ELECTE
DEC 20 1982

E

82 12 20 063

APPLICATION OF SATELLITE-BASED SIDELOOKING RADAR IN MARITIME SURVEILLANCE

by

Einar-Arne Herland

DTIC
COPY
INSPECTED
1

NORWEGIAN DEFENCE RESEARCH ESTABLISHMENT (NDRE)
FORSVARETS FORSKNINGSINSTITUTT (FFI)

POST OFFICE BOX 25
N-2007 KJELLER, NORWAY

REPORT DOCUMENTATION PAGE

1) PUBL/REPORT NUMBER	2) SECURITY CLASSIFICATION	3) NUMBER OF PAGES
NDRE/PUBL-82/1001	UNCLASSIFIED	
1a) JOB REFERENCE	2a) DECLASSIFICATION/DOWNGRADING SCHEDULE	
397/170		110

4) TITLE APPLICATION OF SATELLITE-BASED SIDELOOKING RADAR IN MARITIME SURVEILLANCE
(SATELLITTBÅRET RADARSYSTEM MED SYNTETISK APERTURE FOR HAVOVERVÅKNING)

5) NAMES OF AUTHOR(S) IN FULL (surname first)

HERLAND Einar-Arne

6) DISTRIBUTION STATEMENT

Approved for public release. Distribution unlimited
(Offentlig tilgjengelig)

7) INDEXING TERMS

IN ENGLISH:
a) Synthetic aperture radar
b) Digital processing
c) Autofocusing
d) Target detection
e)

IN NORWEGIAN
a) Syntetisk aperture radar
b) Digital prosessering
c) Autofokusering
d) Måldeteksjon
e)

THESAURUS REFERENCE:

8) ABSTRACT (continue on reverse side if necessary)

The use of a satellite borne synthetic aperture radar (SAR)
system for maritime surveillance is investigated. The system
is analyzed, and algorithms for digital processing of SAR
images from the raw data are developed. These algorithms are
implemented on a general purpose computer and applied to data
from SEASAT-1. An autofocusing algorithm for the azimuth
compression is developed whereby SAR images can be processed
without any additional information on satellite orbit and
attitude. This makes operational use of satellite borne SAR
feasible. A method for target detection from SAR images is
also developed.

9) DATE	AUTHORIZED BY	POSITION
August 23 1982	F Lied	Director

FFI-B-22-1980

CONTENTS

APPLICATION OF SATELLITE-BASED SIDELOOKING RADAR IN
MARITIME SURVEILLANCE
(SATELLITTBÅRET RADARSYSTEM MED SYNTETISK APERTURE FOR
HAVOVERVÅKNING)

SUMMARY

The use of a satellite borne synthetic aperture
radar (SAR) system for maritime surveillance is
investigated. The main advantages of a
synthetic aperture radar are high resolution
combined with all-weather capabilities and
independence of visual sight. The two last
properties are obtained by using a frequency
typically in the area 1 to 10 GHz. The high
resolution is due to the application of the
synthetic aperture principle. Resolution on
the ground is typically 25mx25m, depending
upon system parameters. By using a satellite
platform large areas on the ground can be
covered.

Synthetic aperture radar images can be
obtained by rather extensive digital processing
of the rawdata gathered with the satellite
system. The necessary algorithms to process
such images without use of externally supplied
satellite orbit information have been developed
and are applied to rawdata gathered by the
radar system onboard the SEASAT-1 satellite.
The ability to distinguish ships in such images
is demonstrated, and a target detection
algorithm is developed.

1   INTRODUCTION

A radar operated in pulsed mode is actually a range

measuring instrument. Combined with the angular resolving

capability of the radar antenna, it is possible to

generate an image of an area by means of radar. In one

application the radar antenna rotates and the image is

displayed on a plan position indicator (PPI) where the

radar platform is located in the center of the image.

An imaging radar thus resolves targets in two dimensions.

The resolving properties in range and angle are
principally different, since the range resolution
is given by the bandwidth of the transmitted pulse,
and is thus range independent, while a constant
angle resolution gives a resolution in meters that
is proportional with range.

The resolving power of an antenna is typically
limited by the physical size of the antenna itself.
To overcome this difficulty, Carl Wiley of Goodyear
Aircraft Corporation in 1951 proposed an improvement
in angular resolution by frequency analysis of the
target history obtained with a coherent, moving radar
system. The first experimental demonstration was made
by a group at the University of Illinois in 1953. They
used an airborne radar system at X-band and achieved
an angular resolution that was approximately ten times
better than the resolution of the physical antenna.
The first combat-surveillance system employing an
airborne synthetic aperture radar was successfully
demonstrated by a team from the University of Michigan
in 1957. Since then synthetic aperture radar has been
developed into a very useful instrument for imaging
purposes.

The usual radar platform for synthetic aperture radar
purposes has been an airborne one. In the summer 1978
a satellite called SEASAT-1 was launched which, together
with 4 other instruments, contained a sidelooking radar
designed as a synthetic aperture radar. The purpose of
this satellite was to measure global ocean dynamics and
physical characteristics and to provide monitoring of
ice conditions. It was a proof of concept mission, and
SEASAT-1 was planned to be the first in a series of
similar satellites, and the purpose was to establish
an operacional system. Due to equipment malfunctioning
the satellite failed in orbit after approximately 100

days of operation, and the launching of subsequent
satellites was cancelled. During the time of operation
a considerable amount of data was collected with the
synthetic aperture radar.

This work is concerned with the use of satellite
borne synthetic aperture radar in maritime surveillance.
Although the SEASAT-1 SAR system was not designed for
this purpose, it is shown to be possible to use such
high resolution imagery as can be obtained with this
kind of system for surveillance purposes.

To obtain images from the rawdata collected with a
synthetic aperture radar requires rather extensive
processing. This processing has in the past mainly
been done by means of a coherent optical system. This
is because the large amount of data requires a proces-
sing capacity offered only by optical processing, and
also because film is a convenient storage medium for
the rawdata, thus lending itself naturally to optical
processing.

With the development of digital computers it is now
possible to do real time digital processing for air-
borne synthetic aperture radar, while for a satellite
borne platform this has not yet been demonstrated.

In this work the necessary algorithms for processing,
on a general purpose computer, synthetic aperture
radar images from rawdata gathered by a satellite borne
radar are developed and applied to rawdata from SEASAT-1.
The numerical examples given also use parameters from
the SEASAT-1 SAR system. Of new results, beside the
SAR image processor, which has been developed inde-
pendently of a few c   digital processors, are the auto-
focusing procedu   the method of target detection,
where a tradeoff between resolution and look averaging

is made to maximize the signal to sea clutter ratio
of a target. The autofocusing procedure is very
important in operational use of a SAR system, since
the time delay incurred when using externally supplied
orbit information for the satellite may exclude
operational use of the images.

2 BASIC THEORY

The theory for conventional antennas, both continuous
and array antennas, can be found in (1). Here
will only be given a short outline of a couple of
things that are important to the understanding of
synthetic aperture antennas.

2.1 Array antenna

Figure 2.1 shows the antenna diagram for an array
antenna of seven equally spaced elements, element
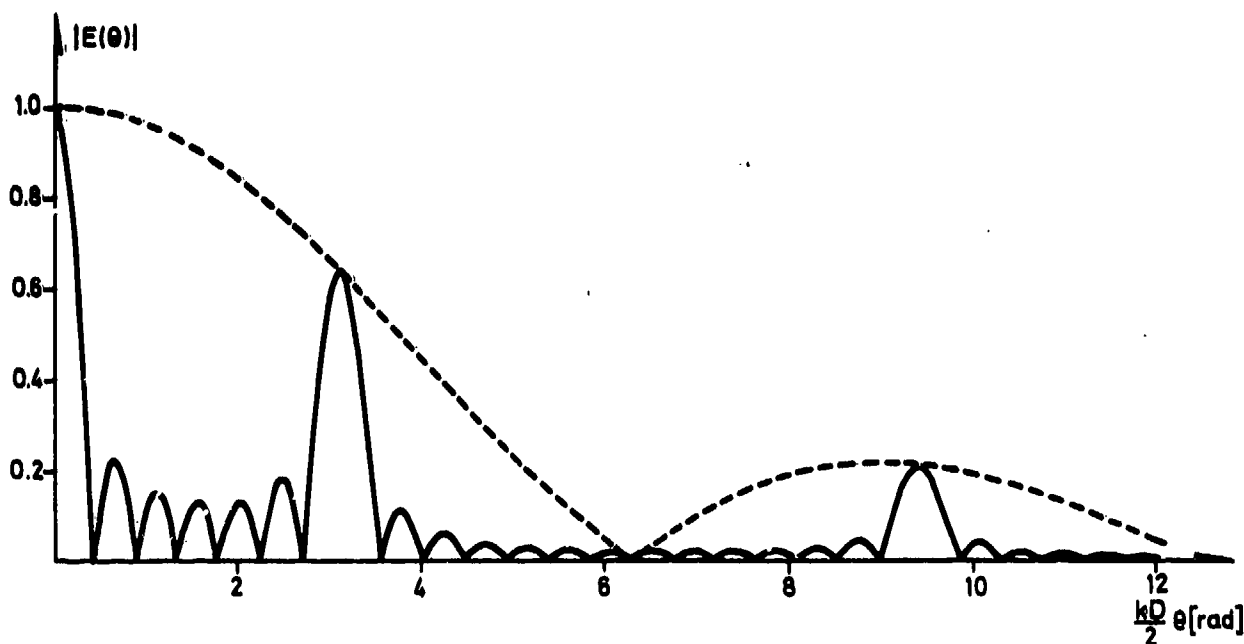length $\frac{D}{2}$ and element spacing D.

Figure 2.1 Antenna diagram for array antenna

The envelope of the diagram is the antenna diagram
of a single element and the major peaks, or grating
lobes, that repeat in angle, stem from the fact that
it is an array antenna. Since a synthetic antenna is

an array antenna, it has a diagram of the same type
as in figure 2.1. The important thing about this
diagram is the grating lobes, which for a synthetic
aperture radar would result in a periodic repetition
in azimuth of every target in the image. When $D > \lambda$,
the transmitted wavelength, the grating lobes appearing
in the main lobe of the envelope can be avoided by
choosing the element length greater than the inter-
element spacing. The corresponding requirement for a
synthetic array antenna is somewhat different and is
given in section 3.2.

An antenna can also be regarded as a spatial filter,
a viewpoint which is useful when studying the analogy
between synthetic aperture radar and holography.

2.2 Synthetic aperture

In a conventional array antenna all the antenna elements
are present simultaneously. In a synthetic aperture
antenna there is only one antenna element. This element
is moved in space to different positions, and in each
position it transmits and receives an electromagnetic
signal. By combining the received signals from different
element positions, a synthetic array antenna is
generated. The geometry is shown in figure 2.2.

A series of different positions of the basic antenna is
shown, together with the antenna beam. A target is
shown, and it is seen that it will be inside the physical
antenna beam for a certain time interval. This time
interval then gives the longest possible synthetic
aperture for the given target. Quantitative relation-
ships will be given in section 3.2. For each antenna
position the pulse echo is coherently recorded, i e the
echo together with a phase reference is stored, and it
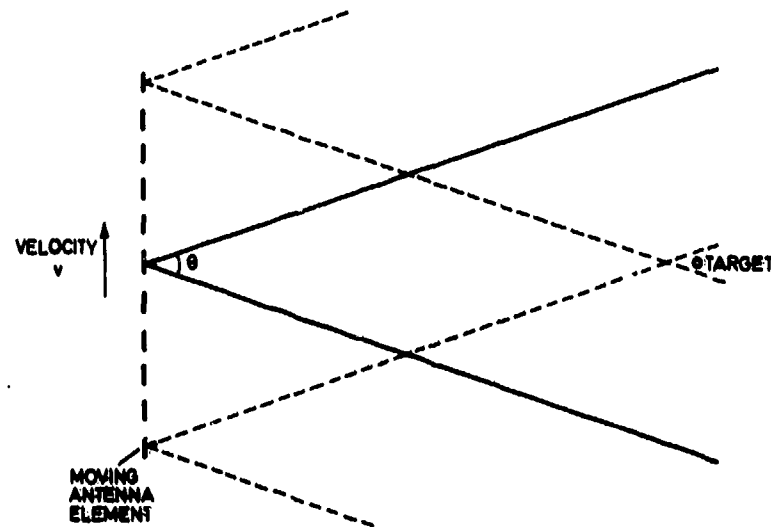
Figure 2.2 <u>Principle for synthetic array antenna</u>

is this phase reference that makes it possible to synthesize an antenna much longer than the physical one.

One difference between a physical and a synthetic array antenna is that in a physical array antenna all the elements receive the echo from the target of a wave transmitted by all the array elements or by a common transmitting antenna, while in the synthetic array each element receives only the echo of the wave transmitted by itself. As will be shown later, this gives the synthetic array two times the phase sensitivity of the corresponding physical array, and the angular resolution for a synthetic array of length D will be the same as the resolution for a physical array of length 2D.

For a target at distance R from the antenna, the longest
possible synthetic aperture is $R \cdot \theta$, where θ is the
beamwidth of the physical antenna. The ground resolution
for the synthetic antenna is then

$$\Delta_s = \frac{1}{2} \frac{\lambda}{R \cdot \theta} \cdot R = \frac{\lambda}{2\theta}$$

If D is the length of the physical antenna, we have

$$\theta = \frac{\lambda}{D} \rightarrow \Delta_s = \frac{D}{2}$$

This shows that the ground resolution of a synthetic
aperture antenna is independent of range and transmitted
wavelength and is equal to half the length of the
physical antenna. The wavelength independence is
valid only as long as $D \gg \lambda$.

2.3   Focused and unfocused antenna

In the previous discussions it has been assumed that
the target is in the far field of the antenna. The far
field extends to infinity, and between the far field,
or Fraunhofer region, and the antenna is the Fresnel
region. The boundary between the Fraunhofer region and
the Fresnel region is rather diffuse, but it can
qualitatively be said that a point target is in the
far field when a spherical wave expanding from the
target can be regarded as plane across the antenna
aperture. This is illustrated in figure 2.3.

Whether an incoming wavefront can be regarded as plane
or not, depends upon the phase difference across the
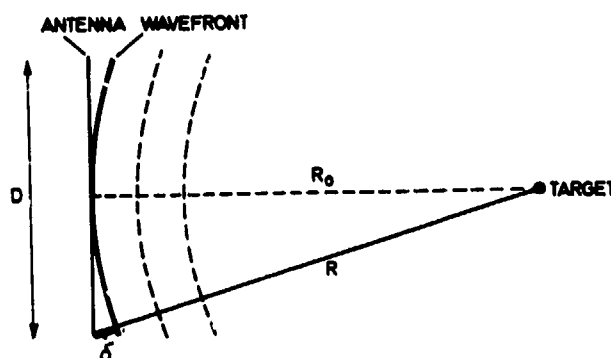
Figure 2.3 <u>Phase variation across antenna aperture</u>

antenna aperture. This phase difference is given by the distance δ in figure 2.3. We have

$$R = R_o + \delta$$

and

$$R = \sqrt{R_o^2 + \frac{D^2}{4}} \approx R_o + \frac{D^2}{8R_o} \quad \text{when} \quad R_o \gg D$$

This gives $\delta = \frac{D^2}{8R_o}$. The corresponding phase difference is

$$\Delta\phi = \delta \cdot k = \delta \cdot \frac{2\pi}{\lambda} = \frac{\pi D^2}{4\lambda R_o}$$

where $k = \frac{2\pi}{\lambda}$ is the wave number of the incoming wavefront. If we require the phase difference across the antenna aperture to be less than $\frac{\pi}{4}$ to regard the wavefront as plane, we have

$$\frac{\pi D^2}{4\lambda R_o} < \frac{\pi}{4} \Rightarrow R_o > \frac{D^2}{\lambda}.$$

This means that a target is said to be in the far field
of the antenna when the distance between the antenna
and the target is greater than $\frac{D^2}{\lambda}$. When the target is
closer to the antenna, it is said to be in the Fresnel
region. When a target is moved into the Fresnel region
of an antenna, there is seen to be destructive inter-
ference along the antenna because of the phase difference
across the antenna aperture. To restore the constructive
interference, the antenna will have to be formed to fit
the wavefront, or in other words one will have to focus
the antenna. For a target lying in the focus of the
antenna, the beamwidth is given by $\frac{\lambda}{D}$ as before. An
unfocused antenna can be thought of as focused at
infinity, and all the targets in the far field can thus
be regarded as being at infinity. To find the actual
ground resolution, however, one has to take into account
the actual distance to the target, since the ground
resolution for an antenna at a distance R is $R \cdot \frac{\lambda}{D}$.

Focusing can be done in two ways. The antenna can be
physically formed to fit the wavefront. One physical
configuration will, however, place the focus in a given
distance from the antenna, and this method is therefore
impractical when one wants to focus at different
distances simultaneously. Another method is to record
separately the returns from the different positions of
the antenna and subsequently focus by signal processing.
In this way one can easily focus at all the distances
one might want. Since this kind of data recording is
inherent in the synthetic aperture principle, this
method is used when generating a focused synthetic
aperture. The processing can be done either optically
or digitally, as will be explained later.

The high processing capacity needed for a synthetic
aperture radar compared to a real aperture radar is
due to the focusing, and not to the principle of

generating a synthetic aperture. Even if a physical
antenna with the same length as the synthetically
generated one should be available, it would require
data recording and processing of the same complexity
as with synthetic aperture because the physical antenna
can only be focused on one distance at a time.

3 SYNTHETIC APERTURE RADAR PERFORMANCE

In this chapter the performance of a synthetic aperture
radar system will be quantitatively evaluated and some
particular phenomena encountered with SAR will be
considered. General descriptions of synthetic aperture
radar can be found in (2) and (3). A satellite borne
system will be considered, a sketch of which is shown
in figure 3.1.
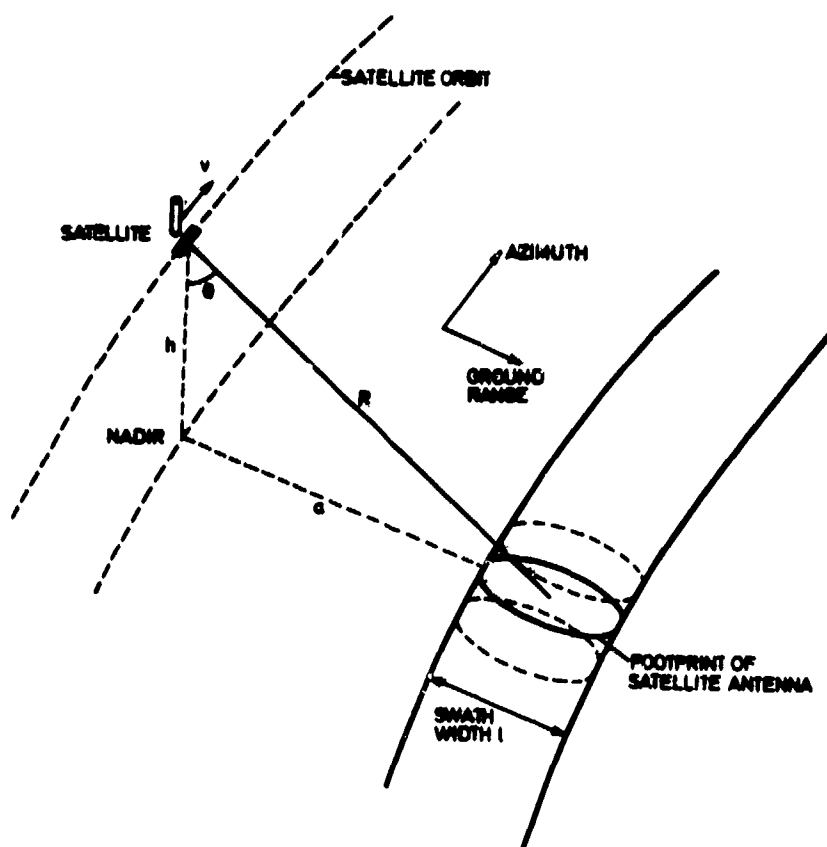
Figure 3.1   Geometry of satellite borne SAR

Approximate values for SEASAT-1 are as follows:

h = 800 km
R = 850 km
a = 240 km
ℓ = 100 km
θ = 20.5°
v = 7 km/sec
Antenna beamwidth in azimuth, 1°
Antenna beamwidth in elevation, 6°

A general description of and detailed parameters for
the SEASAT-1 SAR system can be found in (4).

In the following range resolution will be treated first
and then azimuth resolution.

3.1   Range resolution

Resolution in range with a synthetic aperture radar
is obtained in conventional manner. Although a focused
system has an inherent range resolution given by the
depth of focus, this resolution is highly inferior, as
will be shown later. The range resolution is therefore
obtained by pulsed operation of the radar. This is
shown in figure 3.2 where the flight direction is into
the paper.

If the transmitted pulse bandwidth is B, then the
resolution in radial direction from the antenna is
given by

$$\Delta R = \frac{c}{2B}$$
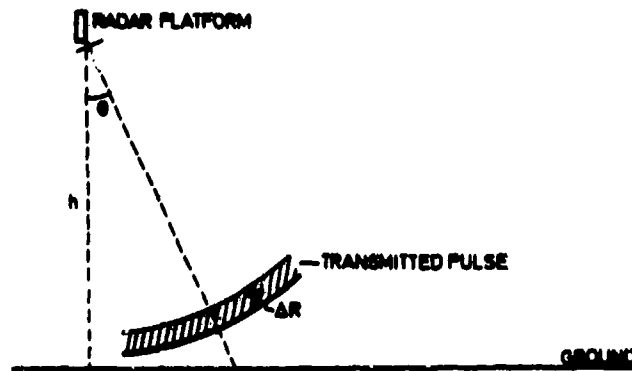
Figure 3.2 <u>Principle of range resolution</u>

where c is the velocity of light. This formula is
valid also when pulse compression techniques are used
(5). The corresponding ground resolution is

$$\Delta R_g = \frac{\Delta R}{\sin\theta}$$

For SEASAT-1 a linear FM-pulse is transmitted, which
gives true range 3 dB resolution $\Delta R = 7.1$ m, where true
range is the distance between antenna and target.
Ground range is the distance from the nadir line to
the target measured on the ground. For SEASAT-1 we
have approximately $17^O < \theta < 24^O$, which gives the
relationship shown in figure 3.3 between R_g and θ. The
lower abscissa axis shows the corresponding ground
range when the satellite's height h = 800 km.

From figure 3.3 it is seen that a processed SAR-image
that is linear in true range will be distorted in such
a way that targets on the ground at near range will
be compressed relative to ground targets at far range.
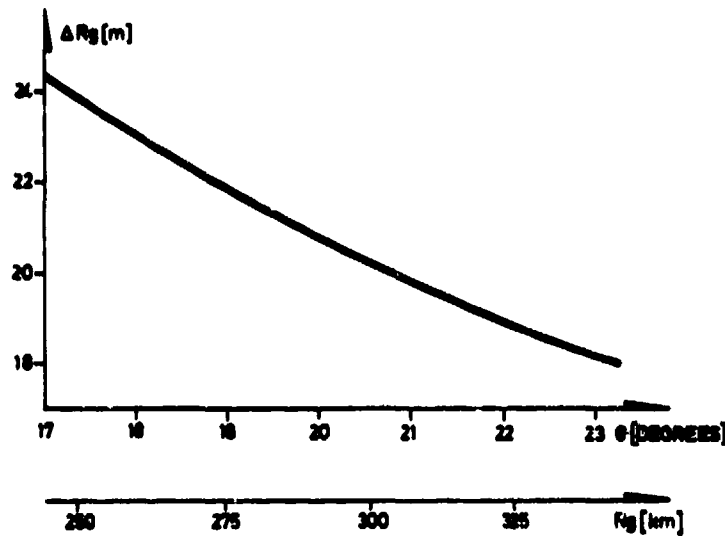
Figure 3.3 Ground resolution as a function of ground range

For SEASAT-1 the transmitted waveform is a linear FM-pulse, which can be written on complex form as

$$s(t) = \exp\{j\pi kt^2\}, \quad -T<t<T$$

The carrier is removed from $s(t)$ above since it does not affect the range resolution. The instantaneous frequency of $s(t)$ is given by the time derivative of the phase $\phi(t)$.

$$f(t) = \frac{1}{2\pi} \cdot \frac{d\phi(t)}{dt} = \frac{1}{2\pi} \frac{d}{dt}(\pi kt^2) = kt$$

The bandwidth of $s(t)$ is thus

$$B = f(T)-f(-T) = 2kT$$

The pulse echo will not be an exact replica of the transmitted pulse because of the relative motion between the antenna and the targets which imposes a

dopplershift on the pulse echo. Figure 3.4 shows a
.socalled squinted system where the boresight direction
makes an angle θ_s with the direction normal to the
flight direction.
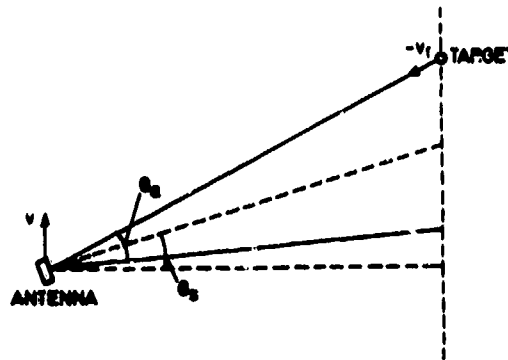
Figure 3.4   Geometry of a squinted system

It is seen that the greatest dopplershift occurs when
the target is on the edge of the beam as shown in
figure 3.4. At this point the relative velocity
between antenna and target is

$$v_r = -v \cdot \sin(\theta_s + \frac{\theta_a}{2})$$

With $r(t) = R_o + v_r \cdot t$, the distance between target and
antenna for the case shown in figure 3.4, the pulse
echo is

$$u(t) = s[t - \frac{2r(t)}{c}] = s(t - \frac{2R_o}{c} - \frac{2v_r \cdot t}{c})$$

The term $\frac{2R_o}{c}$ gives the phase modulation used when
generating the synthetic aperture, but it is constant
for a single pulse echo from one target. It is
therefore removed here. This gives

$$u(t) = s[(1-\frac{2v_r}{c})t] = \exp\{j\pi k(1-\frac{2v_r}{c})^2 t^2\} = \exp\{j\pi k' t^2\}$$

where $k' = k(1-\frac{2v_r}{c})^2 \approx k(1-\frac{4v_r}{c})$ since $v_r \ll c$. The FM-rate k' of the echo pulse is thus slightly different from the transmitted one, depending upon where in the antenna beam the target is, being equal for a target lying normal to the flight direction. The consequences of this depend upon the magnitude of the factor $(1-\frac{4v_r}{c})$. When compressing $u(t)$ with a filter matched to the transmitted pulse $s(t)$, i e with a filter with impulse response $s^*(T-t)$, the normalized output as a function of time delay and the different chirp-rates will be

$$I(k,k';\tau) = \frac{1}{2T}\int_{-T+\tau}^{T} \exp\{j\pi k \cdot t^2\} \cdot \exp\{-j\pi k'(t-\tau)^2\}dt$$

$$= \frac{1}{2T\sqrt{2(k-k')}} \cdot \exp\{-j\pi\frac{kk'}{k-k'}\tau^2\} \int_{\sqrt{2(k-k')}(\frac{k}{k-k'}\tau-T)}^{\sqrt{2(k-k')}(\frac{k'}{k-k'}\tau+T)} \exp\{j\frac{\pi}{2}t^2\}dt$$

$$0<\tau<2T, \ k>k'$$

The value of I for $-2T<\tau<0$ and $k<k'$ is given from the formula above by symmetry. The numerical values of I are given in terms of the Fresnel integrals which are tabulated. By introducing $k_r = \frac{k'}{k}$, $\tau_r = \frac{\tau}{T}$ and $W = 2T \cdot B = 4kT^2$ which is the time-bandwidth product of the linear FM-pulse, we can write

$$I(k_r,\tau_r) = \frac{1}{2\sqrt{\frac{W}{2}(1-k_r)}}\ \exp\{-j\frac{\pi}{4}\frac{k_r}{1-k_r}W\tau_r\}\ \int\limits_{\sqrt{\frac{W}{2}(1-k_r)}\,(\frac{1}{1-k_r}\tau_r-1)}^{\sqrt{\frac{W}{2}(1-k_r)}\,(\frac{k_r}{1-k_r}\tau_r+1)}\exp\{j\frac{\pi}{2}t^2\}dt$$

$$0\leq k_r<1,\quad 0\leq\tau_r\leq2 \qquad (3.1)$$

For $k_r = 1$ we have

$$I(1,\tau_r) = \frac{\sin[\pi\frac{W}{2}\tau_r(1-\frac{\tau_r}{2})]}{\pi\frac{W}{2}\tau_r}\quad,\qquad 0\leq\tau_r\leq2 \qquad (3.2)$$

For SEASAT-1 we have W = 634. $|I(1,\tau_r)|$ is the
magnitude of the response for a perfectly matched
filter and it is shown in figure 3.5. Figure 3.6
shows $|I(k_r,0)|$ which gives the relationship between the
maximum output value of the compression filter and the
relative mismatch in FM-rate between the filter and
the pulse echo.

The maximum mismatch with positive angles will be

$$k_r = (1-\frac{4v_r}{c})^{-1} \approx 1-\frac{4v}{c}\cdot\sin(\theta_s+\frac{\theta_a}{2})$$

The maximum squint angle θ_s for SEASAT-1 is approximately
1°, which together with $\theta_a \approx 1^\circ$ and v $\approx$ 7150 m/s gives

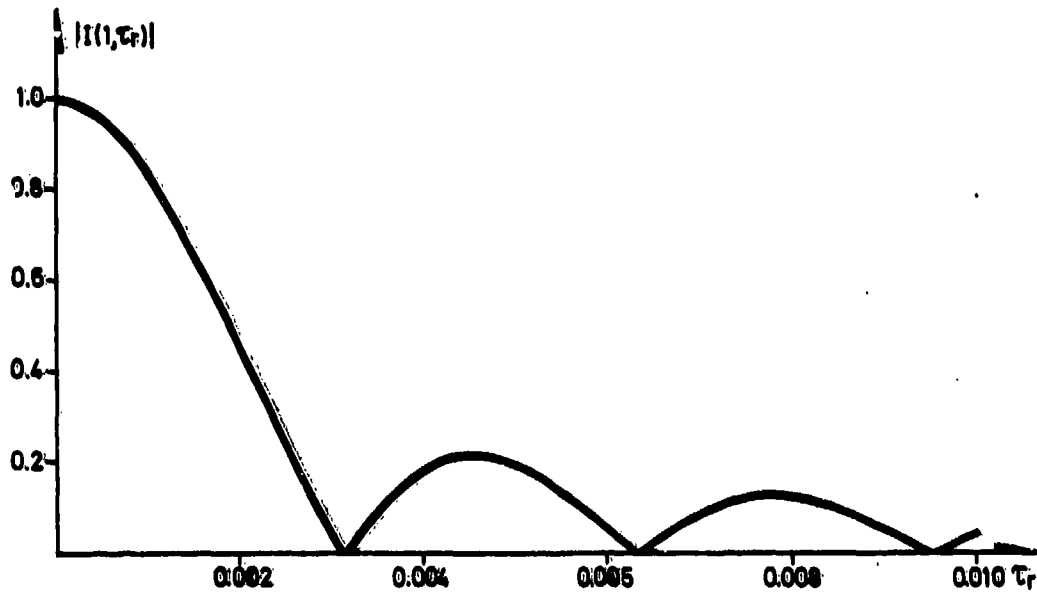$$k_r = 1-2.5\cdot10^{-6}$$

Figure 3.5 <u>Time response for perfectly matched
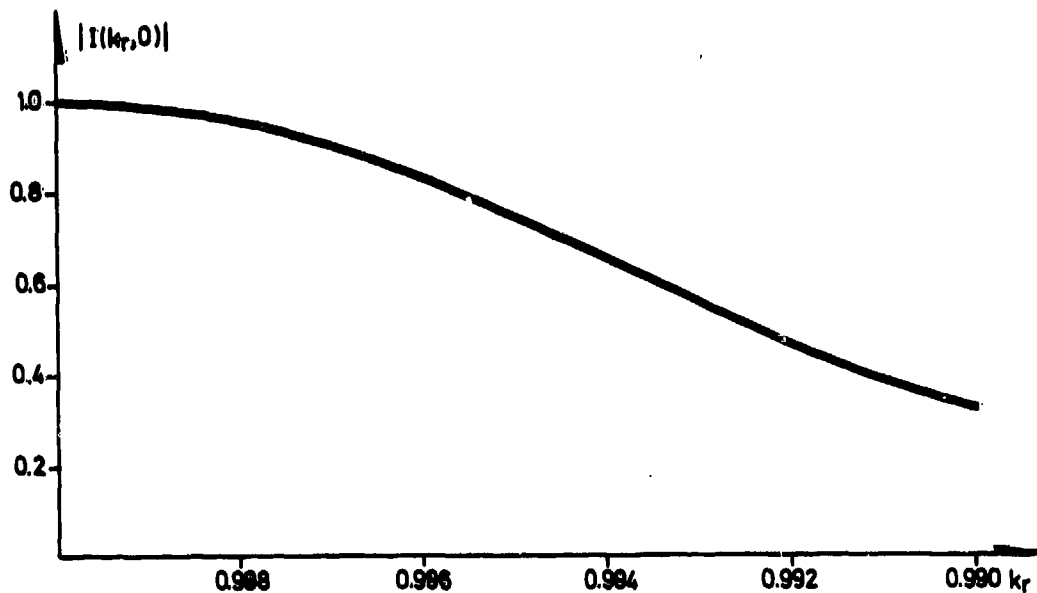compression filter</u>

Figure 3.6 <u>Maximum output of compression filter as
function of FM-rate mismatch</u>

This is seen from figure 3.6 to have negligible effect
on the range compression. If a 1 dB degradation is
set as a limit, this corresponds to $k_r = 0.9968$, which
means that the FM-rate has to be known to 3 decimals.

Another mismatch occurs because of the carrier wave
used when transmitting the pulses. Because of the
relative velocity v_r between antenna and target, the
carrier wave will be dopplershifted an amount $\frac{2v_r}{c} \cdot f$,
where f is the carrier frequency. The maximum doppler-
shift for SEASAT-1 is approximately 1.5 kHz. This will
shift the echo pulse slightly out of the matched filter
bandwidth. Relative to the total bandwidth of 19 MHz
this is $\frac{1.5 \text{ kHz}}{19 \text{ MHz}} = 7.9 \cdot 10^{-5}$, and since the output will
be reduced with the same relative amount, it is
totally negligible.

Since the effects of relative motion between antenna
and targets are negligible, the range compression will
be totally azimuth independent, and can be done
independently of the azimuth compression.

3.2 Azimuth resolution

The basis for generating a synthetic array antenna is
a measure of the distance between the physical antenna
and the target as a function of time. Since this time
history is different for targets at different azimuth
positions, they may be resolved by subsequent processing
of the recorded time histories. Figure 3.7 shows the
physical configuration with a single target.

The position vectors as functions of time, measured
from an arbitrary reference point, are $\vec{x}_a(t)$ for the
antenna and $\vec{x}_t(t)$ for the target. If the antenna
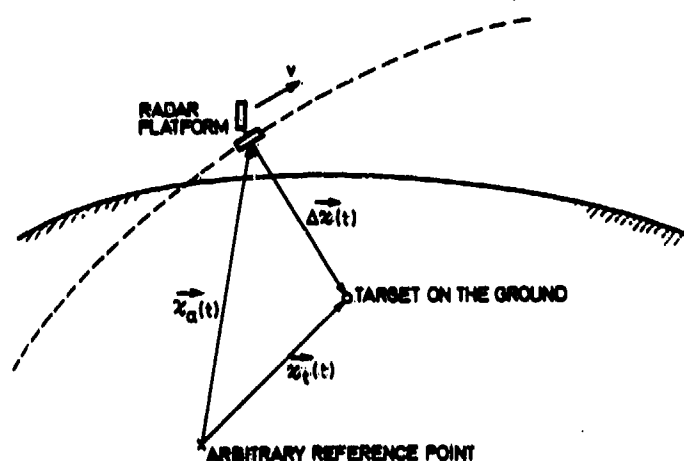
Figure 3.7 <u>Physical configuration with radar and a single target</u>

transmits a continuous monochromatic wave s(t), we have on complex form

$$s(t) = \exp\{j2\pi ft\}$$

where f is the frequency of the transmitted wave. The wave scattered from the target will be

$$u_1(t) = \exp\{j2\pi f[t-\frac{2}{c}|\vec{x}_t(t)-\vec{x}_a(t)|]\} = \exp\{j2\pi f[t-\frac{2}{c}|\Delta\vec{x}(t)|]\}$$

If $u_1(t)$ is coherently demodulated with the transmitted wave, we get

$$u(t) = u_1(t)\cdot\exp\{-j2\pi ft\} = \exp\{-j\frac{4\pi}{\lambda}|\Delta\vec{x}(t)|\}$$

where the transmitted wavelength is $\lambda = \frac{c}{f}$. The measuring of the distance between antenna and target is thus done as a phase measurement, or equally as a time delay measurement.

If the relative movement between antenna and target is
linear, we have the case shown in figure 3.8, where
the target is fixed in space, and the antenna moves
with velocity v.
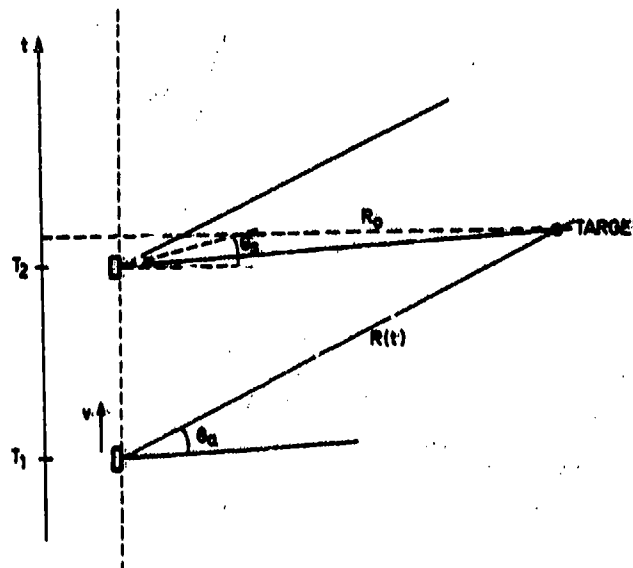
Figure 3.8 Physical antenna in linear motion

In this case we have

$$|\Delta\vec{x}(t)| = r(t) = (R_o^2 + v^2 t^2)^{\frac{1}{2}}$$

The recorded phase history for the target is thus

$$u(t) = \exp\{-j\frac{4\pi}{\lambda}(R_o^2 + v^2 t^2)^{\frac{1}{2}}\} \quad , \quad T_1 < t < T_2$$

where $[T_1, T_2]$ is the time interval when the target is
inside the antenna beam. T_1 and T_2 can be found from
figure 3.8.

$$T_1 = -\frac{R_O}{v}\tan(\frac{\theta_a}{2}+\theta_s) \quad , \quad T_2 = -\frac{R_O}{v}\tan(-\frac{\theta_a}{2}+\theta_s)$$

When θ_a and θ_s are small, and $R_O \gg vT_1, vT_2$, we can use the following approximations

$$\tan x \approx x \text{ and } (1+x^2)^{\frac{1}{2}} \approx 1+\frac{x^2}{2} \text{ when } x \ll 1$$

We then have

$$u(t) = \exp\{-j\frac{4\pi}{\lambda}(R_O+\frac{v^2t^2}{2R_O})\} = C \cdot \exp\{-j2\pi\frac{v^2t^2}{\lambda R_O}\}, \quad C = \exp\{-j\frac{4\pi R_O}{\lambda}\}$$

$$T_1 < t < T_2 \quad , \quad T_1 = -\frac{R_O}{v}(\frac{\theta_a}{2}+\theta_s)$$

$$T_2 = -\frac{R_O}{v}(-\frac{\theta_a}{2}+\theta_s)$$

The factor C in u(t) is a constant for a given target and is of no importance when generating the synthetic aperture.

Since a linear FM-pulse with chirprate k can be written $\exp\{-j\pi kt^2\}$, it is seen that the phase history u(t) for a single target can be approximated with a linear FM-pulse with chirprate $k_a = \frac{2v^2}{\lambda R_O}$. The frequency band actually recorded is given by T_1^O and T_2 above.

The azimuth history can also be thought of as the doppler history of the target as it passes through the antenna beam, since the instantaneous frequency in the azimuth history is equal to the doppler shift caused by the relative motion between antenna and target.

Up to now it has not been considered that the radar
operates in pulsed mode, rather than in continuous
mode. It is the pulsed operation that makes the
synthetic antenna an array antenna, and not a continuous
antenna. The effect of using pulses is equivalent
to sampling the azimuth history of a target with the
pulse repetition frequency (PRF) of the radar.

In section 2.1 it was mentioned that there is a
maximum spacing between adjacent elements in an
array antenna if aliasing effects are to be avoided.
In the case of a synthetic array antenna no aliasing
will occur if the PRF is greater than or equal to the
Nyquist frequency determined by the bandwidth of the
azimuth history. This bandwidth is

$$B_a = k_a \cdot (T_2 - T_1) = \frac{2v^2}{\lambda R_o} \cdot \frac{R_o}{v} \theta_a = \frac{2v}{\lambda} \cdot \frac{\lambda}{D} = \frac{2v}{D}$$

where $\theta_a = \frac{\lambda}{D}$ is used. Since the sampling is complex,
the Nyquist criterion for no aliasing is

$$PRF \geq B_a = \frac{2v}{D}$$

The time T_s between to successive samples then obeys

$$T_s = \frac{1}{PRF} \leq \frac{D}{2v}$$

and the corresponding spatial separation is

$$\Delta_s = v \cdot T_s \leq \frac{D}{2}$$

which means there has to be taken at least one sample
for an antenna displacement equal to half the length
of the physical antenna. In section 3.2.2 this will
be seen to be equivalent to at least one sample per
resolution cell in the azimuth direction.

The effect of undersampling is that each point target will occur in the image for a series of different azimuth positions instead of one.

The synthetic aperture is generated by compression of the azimuth history, in a way similar to the compression in range. Depending upon the complexity of the compression filter, one can discern between unfocused and focused synthetic aperture radar.

3.2.1 Unfocused synthetic aperture

The azimuth history for a target was shown above to be given approximately by a linear FM-pulse

$$u(t) = \exp\{-j2\pi\frac{v^2t^2}{\lambda R_o}\} \ , \qquad T_1 < t < T_2$$

An unfocused synthetic aperture is generated by compressing $u(t)$ with a filter that has no phase corrections. If the length of the synthetic aperture measured in time units is t_u, the azimuth point response is given by

$$a(t) = \int_{t-\frac{t_u}{2}}^{t+\frac{t_u}{2}} u(\tau)d\tau$$

It can be shown that minimum angular 3 dB resolution occurs when $t_u = 1.2 \cdot t_1$, where t_1 is defined by

$$2\pi\frac{v^2t_1^2}{\lambda R_o} = \frac{\pi}{2} \Rightarrow t_1 = \frac{\sqrt{\lambda R_o}}{2v}$$

Figure 3.9 shows a target and a spherical wavefront
emanating from it. Generation of an unfocused
synthetic aperture corresponds to integrating the
incoming wavefront over an area where the wavefront
can be regarded as approximately plane.
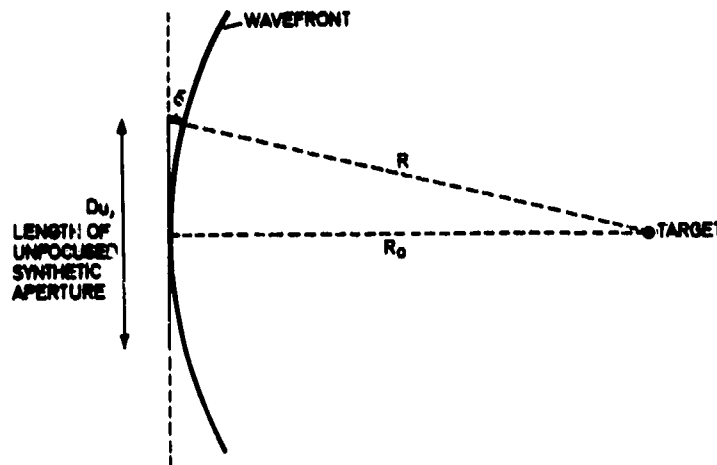
Figure 3.9 _Generation of unfocused synthetic aperture_

To find the resolution obtainable with unfocused
processing, we assume an allowable phase difference
from center to edge of the antenna of $\frac{\pi}{4}$, as was used
in section 2.3 to find the boundary between the
Fresnel and Fraunhofer regions. From section 2.3 we
then have

$$\frac{\pi D_u^2}{4\lambda R_o} = \frac{\pi}{4} \;\Rightarrow\; D_u = \sqrt{\lambda R_o}$$

The ground resolution obtained can be found by considering
the bandwidth of the azimuth history along the synthetic
aperture. This bandwidth is

$$B_u = t_u \cdot k_a = \frac{D_u}{v} \cdot k_a = \frac{1}{v} \cdot \sqrt{\lambda R_o} \cdot \frac{2v^2}{\lambda R_o} = \frac{2v}{\sqrt{\lambda R_o}}$$

Ground resolution is then

$$\Delta_u = \frac{v}{B_u} = \frac{1}{2}\sqrt{\lambda R_o}$$

The antenna diagram for unfocused processing is given by the point response

$$a(t) = \int_{t-\frac{t_u}{2}}^{t+\frac{t_u}{2}} u(t)\,dt = \int_{t-\frac{t_u}{2}}^{t+\frac{t_u}{2}} \exp\{-j2\pi\frac{v^2\tau^2}{\lambda R_o}\}\,d\tau$$

This can be evaluated in terms of Fresnel integrals. The antenna pattern in angle can be found by setting $\theta = \frac{vt}{R_o}$ for small values of θ. Figure 3.10 shows $a(t)$ for different values of t_u, the length of the synthetic aperture in the time domain. $t_1 = \frac{\sqrt{\lambda R_o}}{2v}$ is used as a parameter.

SYNTHETIC APERTURE LENGTH $L_u = v \cdot t_u$

Figure 3.10   Antenna diagrams for different lengths of the unfocused synthetic aperture

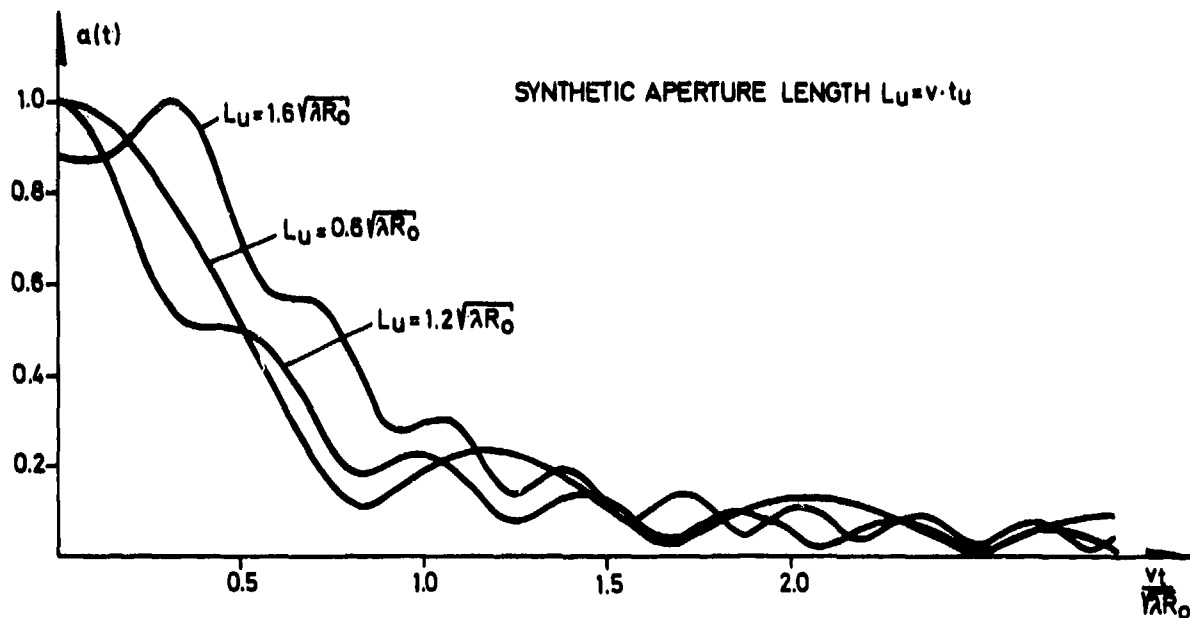### 3.2.2   Focused synthetic aperture

In section 2.3 it was shown that the need to focus an
antenna only arises when the target is in the Fresnel
region of the antenna. The target is said to be in the
Fresnel region when the distance between antenna and
target is less than $\frac{D^2}{\lambda}$, where D is the length of the
aperture. For SEASAT-1 we have $\lambda = 0.24$ m and typically
$D \approx 4$ km, which gives $\frac{D^2}{\lambda} \approx 65000$ km. Since the actual
distance between target and antenna is approximately
850 km, all targets are seen to be deep in the Fresnel
region of the synthetic antenna.

With focused processing the received wavefront is phase
compensated across the whole synthetic aperture. This
is equivalent to matched filtering of the target's
azimuth history. In this case the complete azimuth
history is compressed, and the bandwidth was earlier
found to be

$$B = \frac{2v}{D}$$

This gives ground resolution

$$\Delta_f = \frac{v}{B} = \frac{D}{2}$$

The reason for the range independence of the azimuth
resolution is that while the azimuth bandwidth is
range independent, the time it takes for a given target
to pass through the beam of the physical antenna is
proportional with range. The time-bandwidth product of
the azimuth history is therefore proportional with
range, and the azimuth resolution remains constant.

Since the azimuth history is a linear FM-pulse, the
performance of the azimuth compression is expressed
by formula (3.1). The time-bandwidth product of the

complete azimuth history for SEASAT-1 is approximately
3200. The azimuth antenna diagram without weighting
and with perfect focusing is given by (3.2) with
W = 3200. An actual antenna diagram with weighting
is shown in figure 4.15.

The effect of a focusing error is given by $|I(k_r,0)|$
and is shown in figure 3.11 for W = 3200. If an
azimuth filter matched to targets at range R_o is used
also for targets at range R_1, $R_1 < R_o$, this corresponds
to a focusing mismatch

$$k_r = \frac{2v^2}{\lambda R_o} / \frac{2v^2}{\lambda R_1} \Rightarrow R_1 = k_r R_o$$

From figure 3.11 3 dB degradation is found to give
$k_r = 0.9982$. With $R_o = 850$ km we have $R_1 = 849.065$ km.
This means that the true range interval over which
the same azimuth filter can be used if 3 dB degradation
is tolerated at the edges, is

$$\Delta_r = 2(R_o - R_1) = 1870 \text{ m}$$

The corresponding interval for 1 dB degradation is
$\Delta_r = 1105$ m.

In section 3.4 it will be shown that the normal
processing mode does not compress the whole azimuth
history coherently. If shorter parts of the azimuth
history are compressed coherently and afterwards
incoherently summed, each part will be less sensitive
to focusing errors because of the lower time-bandwidth
products. The case evaluated numerically above can
therefore be regarded as a worst case.
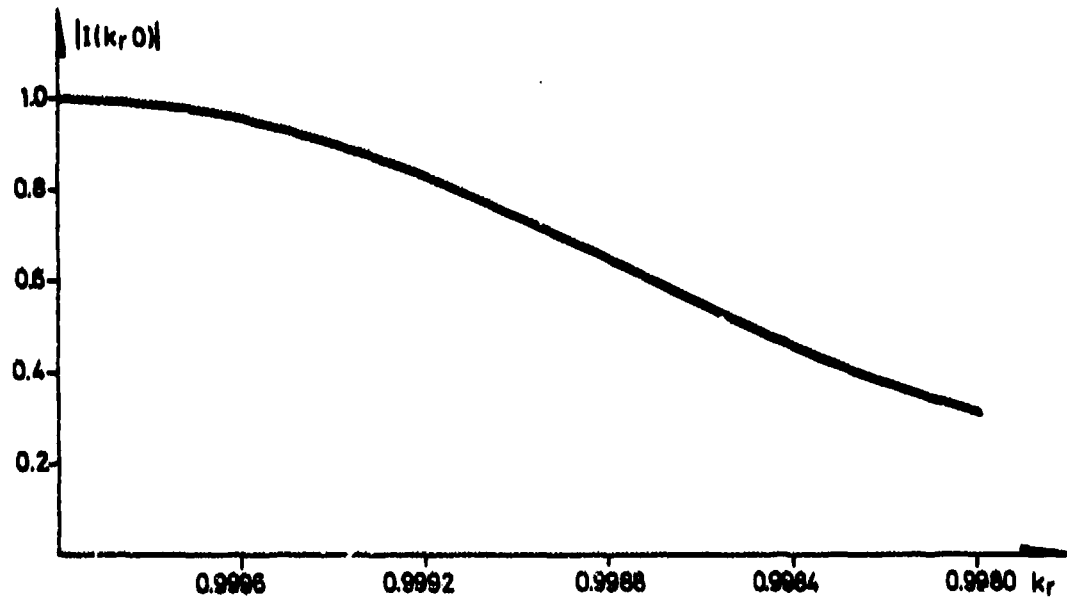
Figure 3.11   Sensitivity to focusing error in azimuth
compression

In section 3.1 it was mentioned that a focused antenna
has an inherent range resolution given by the depth
of focus. This is just the Δ_r calculated above, and
it is seen to be inferior since it is of the order of
kilometers.

The azimuth resolutions that can be obtained with the
types of processing investigated are summarized below
and numerical values for SEASAT-1 are shown.

		SEASAT-1
Real aperture	$\Delta_a = R \cdot \dfrac{\lambda}{D}$	$\Delta_a = 18.2$ km
Unfocused synthetic aperture	$\Delta_a = \dfrac{1}{2}\sqrt{\lambda R}$	$\Delta_a = 223$ m
Focused synthetic aperture	$\Delta_a = \dfrac{D}{2}$	$\Delta_a = 5.5$ m

3.3   Image distortions and artifacts

There are different kinds of distortions that appear
in a synthetic aperture radar image of an area on
the ground. These can be divided into deterministic
and stochastic distortions, although the distinction
between these two is partly a matter of definition.

The simplest type of distortion is the purely geometric
distortion which gives a scale distortion, in general
nonlinear, of the image. This kind of distortion was
mentioned in section 3.1, where the difference between
ground range and true range was treated. Similar
distortions may also occur in the azimuth coordinate
depending upon how the azimuth filters are generated.
This is a correctable distortion, since it only causes
a warping of the coordinate system in the processed
image. It will not be treated here, since the absolute
locations of targets in an image is of little
importance for the purposes considered here.

First a type of distortion called range fold-over is
treated. Then imaging of moving targets is studied.
At last stochastic errors are briefly considered.

3.3.1   Range fold-over

Range fold-over is a distortion that stems from the
difference between true range and ground range.
Figure 3.12 shows a mountain and the way it will
appear in the image.

All the three points A, B and C are at the same true
range from the radar and will therefore be mapped to
the same image point. This has the effect of folding
the mountains towards the radar.
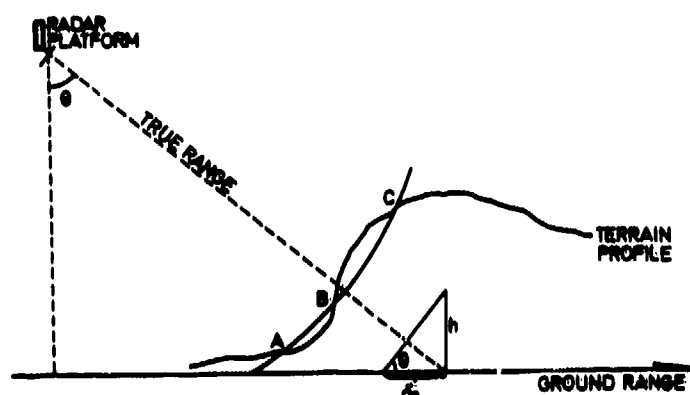
Figure 3.12 Example of range fold-over

The displacement for an object at height h from its
correct ground range position is approximately, from
figure 3.12,

$$\delta_r = h \cdot \cot\theta \quad , \quad \text{for SEASAT-1} \quad \delta_r \approx h \cdot \cot 20^\circ \approx 2.7 \, h$$

This type of distortion is incorrectable and is easily
seen in images of mountainous areas, as for example in
figure 4.22.

3.3.2 Moving targets

As shown earlier, the principle of generating a synthetic
aperture is based on relative movement between target
and radar platform. When imaging the surface of the
earth, a target that is in motion relative to the surface
will be imaged differently from a target that is
fixed on the surface. This will for example be the
case for a moving ship, and even for the sea itself
although the motion of the sea surface to a high degree
may be considered as stochastic.

It was shown in section 3.1 that the dopplershift caused by a moving target is of no concern in range compression. The only effect of a moving target therefore appears in the azimuth compression.

It was shown in section 3.2 that the recorded phase history for a target is

$$u(t) = \exp\{-j\frac{4\pi}{\lambda}|\vec{r}(t)|\}, \quad T_1 < t < T_2$$

where $\vec{r}(t)$ is the relative displacement vector between antenna and target. For quasi-linear relative motion we have

$$|\vec{r}(t)| = (R_o^2 + v^2 t^2)^{\frac{1}{2}}$$

It is convenient to divide the target motion into components in range direction and azimuth direction. There will also be a component normal to both the range and azimuth directions, but this can be neglected for all targets of interest.

If terms of higher order than second are neglected, the motion of a target relative to the ground in the coordinates mentioned above can be described by four parameters, v_r, v_a, a_r and a_a, where v is velocity and a acceleration, and the indices are r for range and a for azimuth. The length of the displacement vector for a moving target can then be written

$$|\vec{r}(t)| = \{[R_o + v_r \cdot t + \frac{1}{2}a_r t^2]^2 + [(v+v_a)t + \frac{1}{2}a_a t^2]^2\}^{\frac{1}{2}}$$

By retaining terms up to second order in time, we get

$$|\vec{r}(t)| \approx R_o + v_r \cdot t + \frac{1}{2}[a_r + \frac{(v+v_a)^2}{R_o}]t^2$$

The corresponding phase history is

$$\phi(t) = \frac{4\pi}{\lambda}|\vec{r}(t)| = \frac{4\pi}{\lambda}\{R_0 + v_r \cdot t + \frac{1}{2}[a_r + \frac{(v+v_a)^2}{R_0}]t^2\}$$

We see that with the approximations made here, the acceleration a_a in the azimuth direction has no impact on the processing.

The difference in phase history between a moving target and a stationary target is

$$\Delta\phi(t) = \frac{4\pi}{\lambda}\{v_r \cdot t + [\frac{1}{2}a_r + \frac{v \cdot v_a}{R_0}]t^2\}$$

where the approximation $2v \cdot v_a + v_a^2 \approx 2v \cdot v_a$ has been used since $v \gg v_a$.

The term $v_r \cdot t$ represents a frequency shift in the azimuth history of $-\frac{2v_r}{\lambda}$ Hz. Since the azimuth history of a target is approximately a linear FM-pulse, this means that the effect of the velocity component v_r is a displacement of the target in the processed image in azimuth direction.

The effect of a_r and v_a is to change the chirprate of the azimuth history. The chirprate for a stationary target is $k = \frac{2v^2}{\lambda R_0}$, and for a moving target we get chirprate

$$k' = \frac{4}{\lambda}(\frac{1}{2}a_r + \frac{v \cdot v_a}{R_0}) + k$$

Expressed in relative terms we have

$$k_r = \frac{k}{k'} = (\frac{R_0 a_r}{v^2} + \frac{2v_a}{v} + 1)^{-1}$$

The effect of this mismatch is to cause defocusing of the target in the image.

The velocity component v_r may also have another
impact on the processing since it changes the target
trajectory in the raw data. Since the trajectory is
oriented mostly in the azimuth direction, it is very
little sensitive to v_a. The change in trajectory will
cause a smear of the target in the image.

The extra range migration for a moving target during
the generation of the synthetic aperture is

$$\Delta R = v_r \cdot \frac{\lambda}{D} \cdot R_o \cdot \frac{1}{v} = \frac{v_r}{v} \cdot \frac{\lambda R_o}{D}$$

where D is the length of the real antenna. $\frac{\lambda R_o}{D}$ is
the length of the synthetic aperture.

The quantitative effects of these distortions are given
below in terms of numerical values for SEASAT-1.

The dopplershift in the azimuth history due to the
radial velocity v_r was above found to be $-\frac{2v_r}{\lambda}$ Hz, where
v_r is positive away from the radar. The dopplershift
caused by a stationary target as it passes through the
antenna beam is continuously decreasing. If a moving
target causes an extra dopplershift, this corresponds to
a target appearing earlier if the extra dopplershift is
negative, and to a target appearing later if the
dopplershift is positive. The displacement of the
target in the image will therefore be as shown in
figure 3.13.

An example of this phenomenon is shown in figure 3.14,
where several ships moving in the radial direction
are shown. The wake shows the direction of the ship's
movement and where it actually is. The azimuthal
displacement of the ships themselves is clearly seen
from the figure. In figure 3.15 ships moving in the
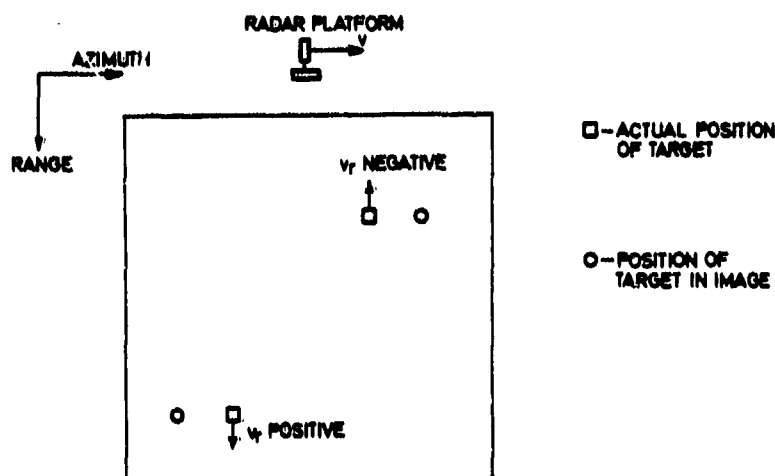
Figure 3.13   Displacement in image of radially moving
              target

azimuth direction are shown, and no displacement from
the wake is seen to occur.

A displacement in azimuth with one resolution cell,
i e 25 m, gives

$$\frac{2v_r}{\lambda} \cdot \frac{1}{k_a} \cdot v = 25 \text{ m}$$

where k_a is the azimuth chirp rate. Typical values for
SEASAT-1 are $k_a \approx 500$ Hz/sec and $v \approx 7000$ m/s, and we
get

$$v_r \approx 0.2 \text{ m/s}$$

With a depression angle of 70°, the corresponding
ground range velocity is

$$v_g = v_r/\cos 70^{\circ} \approx 0.65 \text{ m/s} = 1.3 \text{ knots}$$
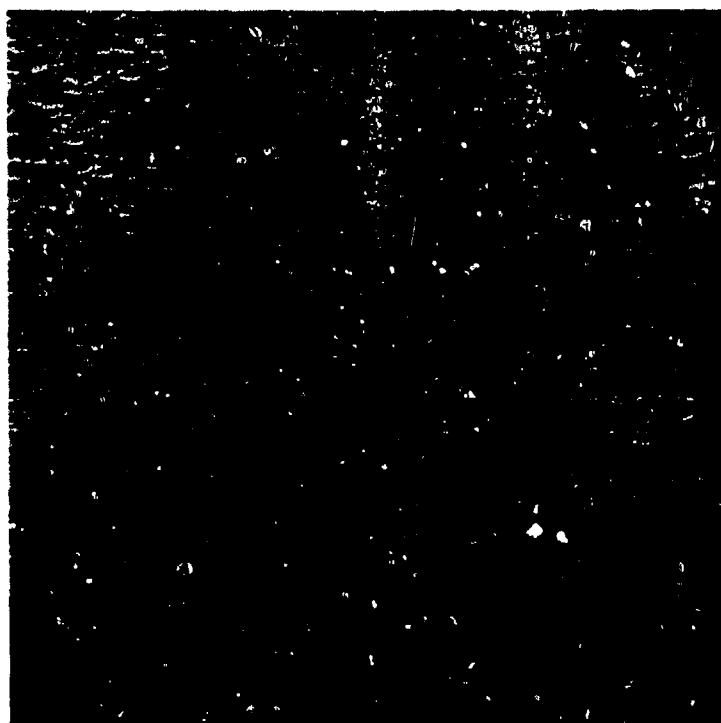
Figure 3.14   Radially traveling ships
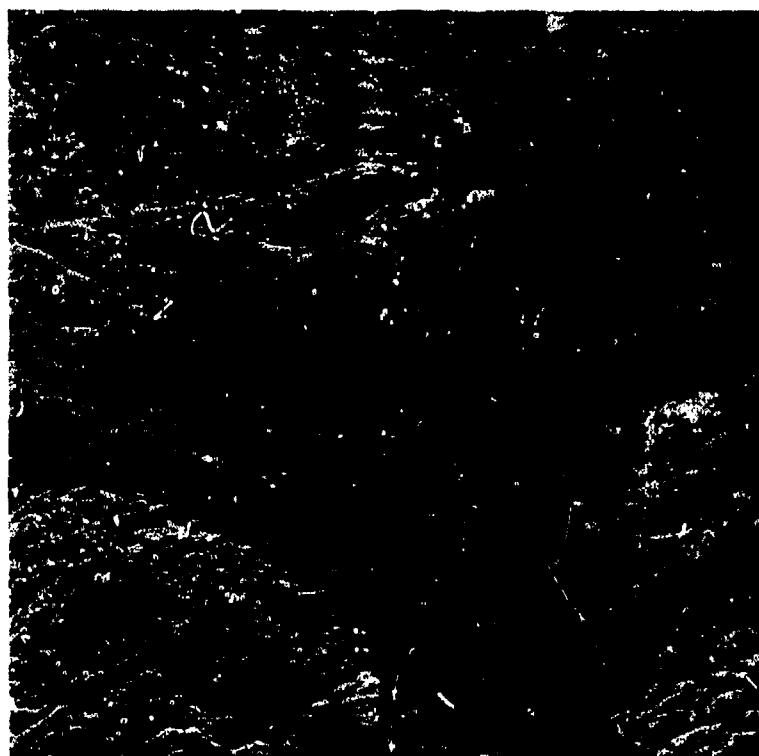
Figure 3.15   Azimuthally traveling ships

Typical displacements in figure 3.14 correspond to velocities of approximately 15 knots, which is seen to be quite reasonable.

Smearing in the image caused by v_r is said to occur when the radial displacement during the synthetic aperture is greater than one range resolution cell. This is approximately 8 m for SEASAT-1 and gives

$$\frac{v_r}{v} \cdot \frac{\lambda R_o}{D} > 8 \text{ m}$$

$D = 11$ m, $v = 7000$ m/s and $R_o = 850$ km gives

$v_r > 3.1$ m/s ≈ 6 knots

Corresponding ground velocity is

$v_g > 18$ knots

In section 3.2 it was found that a mismatch in focus corresponding to $k_r = 0.9989$ gives a 3 dB degradation in peak response. It was found above that the components a_r and v_a give a mismatch in focus corresponding to

$$k_r = (\frac{R_o a_r}{v^2} + \frac{2v_a}{v} + 1)^{-1}$$

With $R_o = 850$ km and $v = 7000$ m/s we have

$k_r = 0.9989$ and $a_r = 0 \Rightarrow v_a = 3.9$ m/s $= 7.6$ knots

$k_r = 0.9989$ and $v_a = 0 \Rightarrow a_r = 0.06$ m/s^2, $a_g \approx 0.2$ m/s^2

Since an acceleration of 0.2 m/s^2 is very high for a
ship target, defocusing is likely to be due to the
azimuthal velocity component v_a.

The numerical results derived above are summarized below.
All velocities are ground velocities.

Azimuth displacement	v_r > 1.3 knots
Smearing in range	v_r > 18 knots
Azimuth defocusing	v_a > 7.6 knots

If the azimuthal displacement from the wake is used
to estimate the ship's radial velocity, v_r = 1.3 knots
can be regarded as the velocity resolution.

3.3.3   Stochastic errors

Some of the errors can only be modelled as stochastic
errors, and the effects expressed in terms of mean
values, variances and correlation functions. The most
important of this type of errors can be expressed as
phase errors in the azimuth history of a target. If the
azimuth history of a target is written

$$u(t) = a(t) \cdot \exp\{-j \cdot \phi(t)\}$$

where $a(t)$ is the amplitude and $\phi(t)$ is the phase
history of a target, then a phase error $\delta\phi(t)$ can
be included by writing

$$u(t) = a(t) \cdot \exp\{-j[\phi(t) + \delta\phi(t)]\}$$

Fluctuations in $a(t)$ have been neglected since they are
in general of less importance than $\delta\phi(t)$. The phase
error term $\delta\phi(t)$ includes random propagation delay

through the atmosphere, phase jitter in the applied
signals and random motions of targets and platform. The
effect of $\delta\phi(t)$ on the compression operations will depend
upon the statistical properties of $\delta\phi(t)$. This type of
errors is not analyzed here, but references (6) and (7)
contain results from investigations of such errors.

3.4   Speckle reduction

Because a synthetic aperture radar system is a highly
coherent imaging system, the images generated are
subject to speckle (8), (9). This phenomenon, which
gives the images a granular appearance, can be explained
by means of figure 3.16. This figure shows a single
resolution cell on the ground, where its projection
in true range is considered. Several specularly
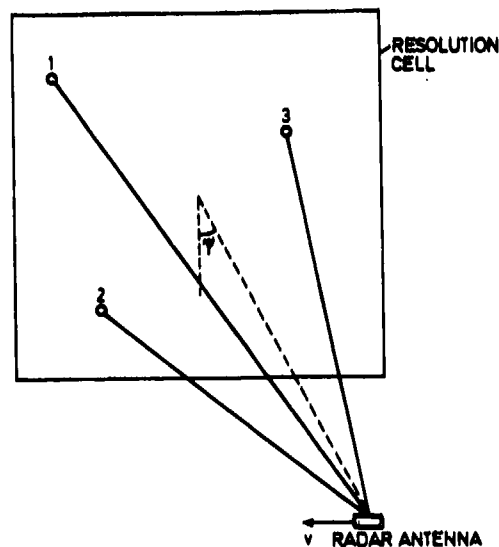reflecting elements inside the resolution cell are
shown.

Figure 3.16   Speckle in coherent imaging systems

If the signals received at the radar are designated

$A_i \cdot \exp\{j\phi_i\}, \quad i = 1,2,3$

where ϕ_i includes both propagation delay and the internal phase of the scattering elements, the complex amplitude at the receiver will be

$$a(\psi) = \sum_{i=1}^{3} A_i \cdot \exp\{j\phi_i\}$$

where the dependency upon the viewing angle ψ has been explicitly denoted. ψ has a one-to-one correspondence with the azimuth time coordinate, and the received signal is therefore seen to vary in time in a manner determined by the spatial locations of the scattering elements inside the resolution cell.

In the general case with N scattering elements inside the resolution cell the received signal will be

$$a(\psi) = \sum_{i=1}^{N} A_i \cdot \exp\{j\phi_i\}$$

and both A_i and ϕ_i, and consequently $a(\psi)$, can be regarded as random variables.

If all the A_i's and ϕ_i's are statistically independent and the ϕ_i's are uniformly distributed on the interval $[-\pi, \pi]$, the addition of the complex amplitudes at the receiver can be regarded as a random walk in the complex plane (9). If the number N of scattering elements is high, this process is similar to the narrowband noise process, and the probability distribution of $|a(\psi)|$ is equivalent to the distribution of the amplitude of narrowband noise, i e the Rayleigh distribution. We thus have

$$p(|a|) = \frac{2|a|}{a_o^2} \exp\{-\frac{|a|^2}{a_o^2}\} \quad , \quad |a| > 0$$

where $a_o^2 = <|a|^2> = \int_0^\infty |a|^2 p(|a|)d|a|$

The intensity of the received signal is $I(\psi) = |a(\psi)|^2$, the distribution of which is exponential

$$p(I) = \frac{1}{I_o} \exp\{-\frac{I}{I_o}\} \qquad (3.3)$$

where $I_o = <I>$ is the expected value of the intensity.

The geometry shown in figure 3.16 is not directly applicable to the case of synthetic aperture radar, since each resolution cell is imaged by means of a synthetic aperture extending over an interval of the viewing angle ψ. If, however, this imaging process is thought to occur separately for each scattering element inside the resolution cell, the resulting signal can be assigned for example to the midvalue of the ψ-interval, and the geometry will be applicable also to the SAR case.

The assumptions about the statistical properties of the scattering elements, which are characteristic of what is called fully developed speckle, can not be expected to hold for very strong targets, as for example urban areas on land and ships on the sea. For most land areas and for the sea surface, however, the assumptions will in general be well satisfied. A resolution cell of 25mx25m on the sea surface will contain many independent scattering elements, and with a radar wavelength of 23.5 cm the phase execursions over the resolution cell will be large enough to give uniform phase distribution.

An example of an image of a sea area is shown in figure 3.17, where the speckly nature of the image clearly can be seen. Figure 3.18 shows the probability distribution function of the intensity calculated from the image and also the theoretical distribution according to formula (3.3) where the mean intensity calculated from the image has been used. They are seen to be in excellent agreement with each ohter.

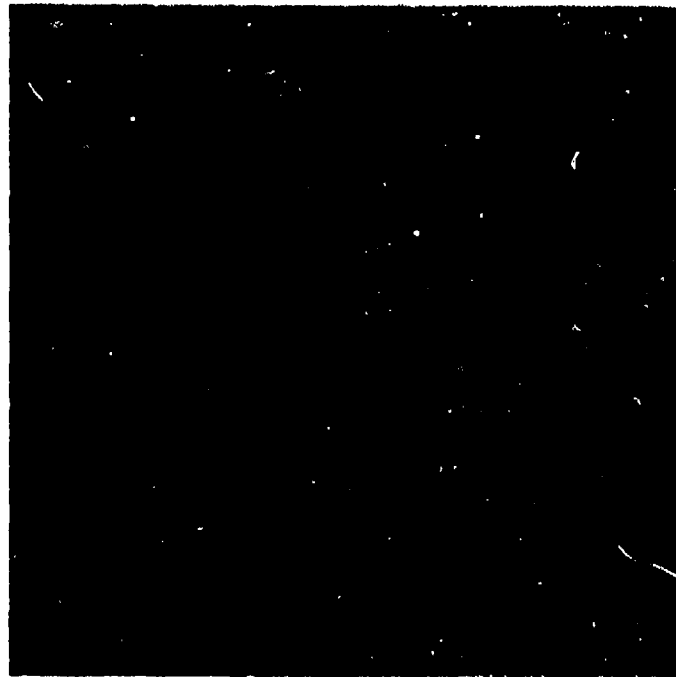Figure 3.17 Image of sea area showing speckle

As mentioned above the speckle in the images is caused by the coherence of the imaging process. The speckle effect can be reduced if several uncorrelated images of the same ground area are generated and afterwards incoherently added, that is added on an intensity basis.

The contrast of a speckle pattern is defined as

$$C = \frac{\sigma_I}{I_o}$$
(3.4)

THEORETICAL DISTRIBUTION IS FULLY DRAWN
DOTS ARE VALUES CALCULATED FROM IMAGE
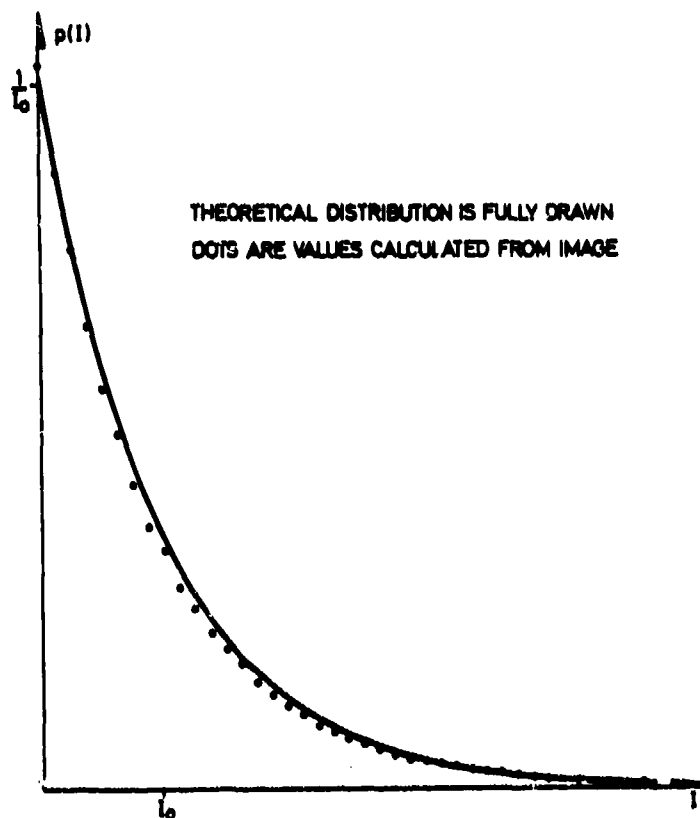
Figure 3.18 Intensity distribution for image in figure 3.17

i e the ratio between the standard deviation and the mean value of the intensity. With the probability distribution given in (3.3) we get $C = 1$. Addition of N uncorrelated images gives a contrast $1./\sqrt{N}$.

The formulas above are for polarized speckle. By using two orthogonal polarizations two uncorrelated images are obtained. The usual method for obtaining uncorrelated images, and the one used here, is to generate images from different parts of the signal spectra. These images will be uncorrelated if they occupy nonoverlapping parts of the spectrum. This method represents a compromise between resolution and speckle reduction.

The twodimensional signal spectrum is shown in figure
3.19, where it is divided into N_r equal frequency bands
in range and N_a bands in azimuth.
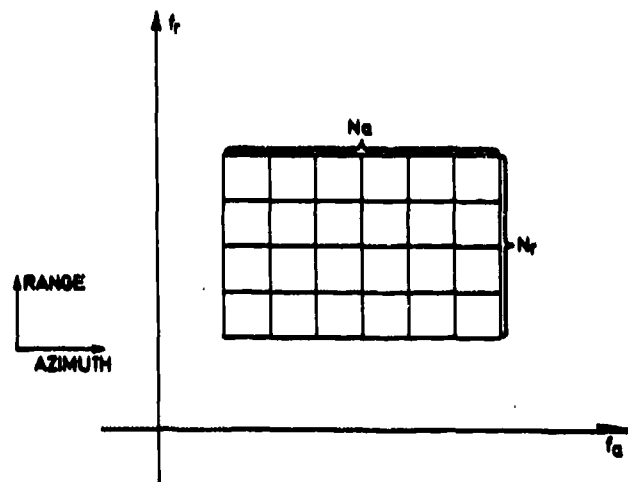
Figure 3.19   Division of signal spectrum in equal
              frequency bands

This will give $N_r \cdot N_a$ uncorrelated images. If the best
resolutions that can be obtained by the system are Δ_r
in range and Δ_a in azimuth, which corresponds to $N_r =
N_a = 1$, this procedure gives resolutions $N_r \cdot \Delta_r$ and
$N_a \cdot \Delta_a$, and a speckle contrast $1/\sqrt{N_r \cdot N_a}$.

In the case of SEASAT-1 we use $N_r = 1$ and $N_a = 4$. This
gives a resulting ground resolution of approximately
25mx25m and a speckle contrast of 0.5. Since the
azimuth history is a linear FM-pulse, the different
frequency bands correspond to different time sections
as shown in figure 3.20.

Each of the sections is called a "look". Since each
look represents a particular viewing angle, uncorrelated
images are seen to be obtained by angular diversity.
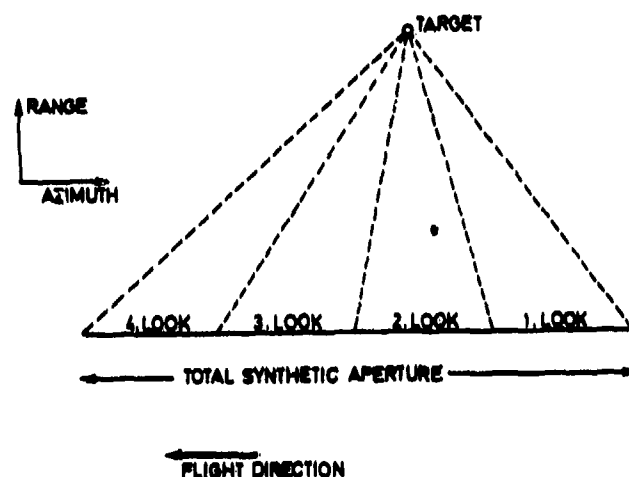
Figure 3.20 Generation of 4 uncorrelated looks

Partially overlapping looks will give a look correlation that depends upon the degree of overlap. The images processed here have the four looks placed in the time domain as shown in figure 3.21.
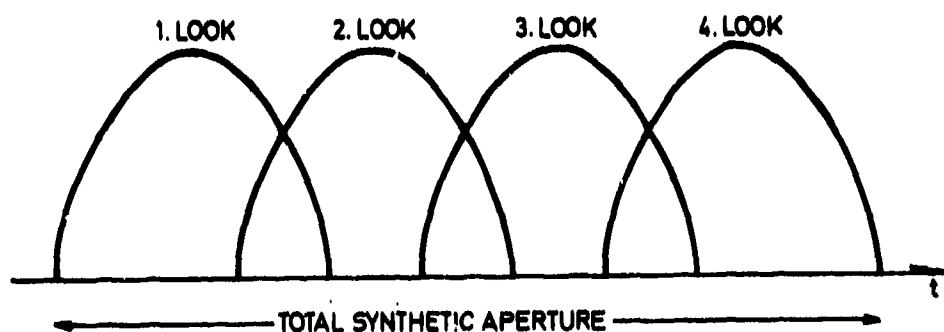
Figure 3.21 Four partially overlapping looks

The window functions used for the looks are shown, and neighbouring looks have 1/3 overlap on the time axis. Because of the window functions, the effective overlap

will be less than 1/3. The lowest curve in figure
4.25 shows that a contrast of very nearly 0.5 is
obtained in this way for a sea area, which shows that
the 4 looks are nearly uncorrelated.

Figure 3.22 shows the four different looks for an area
in the Strait of Dover, and figure 3.23 shows the effect
when adding the looks together. The reduction in
speckle when averaging looks is easily seen.

First look

Second look

Third look

Fourth look

Figure 3.22   Four different looks of the same area

1 look   2 looks
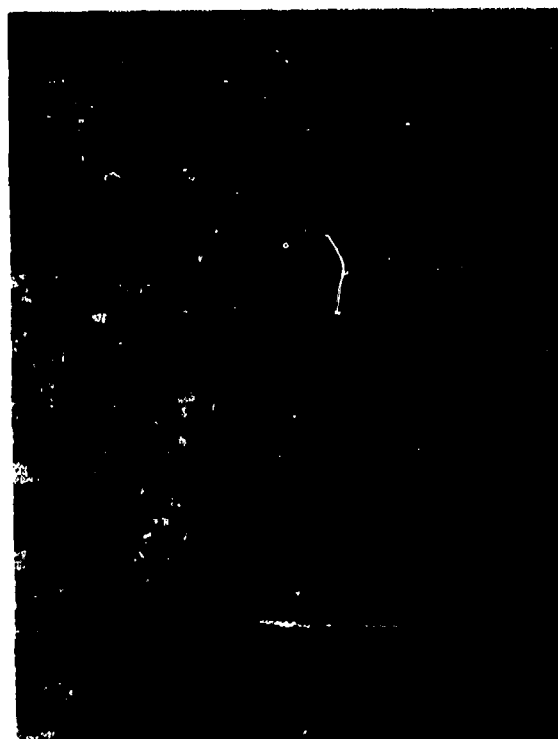
3 looks   4 looks

Figure 3.23 Effect of look averaging

4 PROCESSING OF SYNTHETIC APERTURE RADAR IMAGES

Processing of SAR images from rawdata consists of
matched filtering of the rawdata with a filter
matched to the point target response. This is a
twodimensional filtering operation in range and
azimuth.

When generating a SAR image, the last operation is
conversion from complex amplitude representation of
the signals to intensity. Although this is a
nonlinear operation, the quality of the image is
well described by signal to noise ratios before
intensity conversion because all the preceding
operations are linear filtering operations.

The received power can be found from the radar
equation. If the scattering cross section of a
resolution cell on the ground is $A \cdot \sigma_o$, where A is
the area of the resolution cell and σ_o is the radar
reflectivity, the received power is

$$P_r = \frac{P_t \cdot G^2 \cdot \lambda^2 \cdot A \cdot \sigma_o}{(4\pi)^3 \cdot R^4}$$

where P_t is transmitted power and G is antenna gain.
The system noise power is

$$N = kTB$$

where k is Bolzmann's constant, T is effective noise
temperature and B is receiver bandwidth. For SEASAT-1
we have

$P_t = 800$ W
$G = 35$ dB
$T = 650$ K
$B = 19 \cdot 10^6$ Hz
$R = 850$ km

For 1 look and full resolution we have $A \approx 150$ m^2 which gives signal to noise ratio

$$\frac{P_r}{N} = \frac{P_t \cdot G^2 \cdot \lambda^2 \cdot A \cdot \sigma_o}{(4\pi)^3 \cdot R^4 \cdot k \cdot T \cdot B} = 3.8 \cdot 10^{-4} \cdot \sigma_o = -34 \text{ dB} + \sigma_o [\text{dB}]$$

For an average sea model we have in the middle of the swath (4), $\sigma_o = -14$ dB which gives

$$\frac{P_r}{N} = -34 \text{ dB} - 14 \text{ dB} = -48 \text{ dB}$$

The processing gain is given by the time-bandwidth products of the range and azimuth waveforms, 634 in range and approximately 3200 in azimuth. Processing gain is then

$$G_p = 634 \cdot 3200 = 2.03 \cdot 10^6 \approx 63 \text{ dB}$$

This gives a resulting signal to noise ratio of 63 dB - 48 dB = 15 dB.

Processing of SAR images has in the past mainly been done by optical processing, where a configuration of lenses and a coherent light source are employed. The rawdata signal is stored on film in a twodimensional format, the optical system scans this input film and the output is images which also are recorded on film.

The main reasons for doing the processing optically are processing speed, the suitability of film as a storage medium for large amounts of rawdata, and the fact that the azimuth signal for a target, used for generation of the synthetic aperture, exhibits self focusing properties in a coherent optical system.

Descriptions of signal formats and optical configurations
used for optical processing of SAR images can be found
in (10) and (11).

4.1 Digital processing

Although optical processing of SAR images still is
used when really great throughput is needed, digital
processing has some important advantages. The optical
configuration needed is not very mobile and the optical
recorder needed for recording the rawdata signal on
film is a critical element. These are avoided with
digital processing, and the ease with which processing
parameters can be adjusted and optimized in digital
processing tends to give digitally processed images
higher quality than optically processed ones.

The SAR in SEASAT-1 was an L-band radar operating at
1.275 GHz. The pulse echoes were upconverted to S-band
before transmission to ground. After reception on
the ground the echoes were demodulated and converted
to 5 bit samples and stored on magnetic tape.

The data recording is a twodimensional sampling
operation, sampling in azimuth by transmission of
pulses and in range by the A/D-conversion mentioned
above. The sampling frequency depends upon whether
the sampling is real or complex. If the azimuth
sampling is complex, this gives a PRF that is only
half the corresponding real sampling frequency, and
it also makes it possible to use a recording window
that has the double length of what it has in the case
of real sampling. For SEASAT-1 the sampling is
complex. An explanation of differences between these
modes of operation can be found in (12).

The twodimensional filtering that has to be
accomplished is performed digitally by doing two
onedimensional filtering operations, one in range
and one in azimuth.

It is convenient to consider the recorded radar
echoes as a twodimensional signal, and in the case
of optical processing this is actually done when
recording the signal on film. A similar format when
using digital processing is shown in figure 4.1.
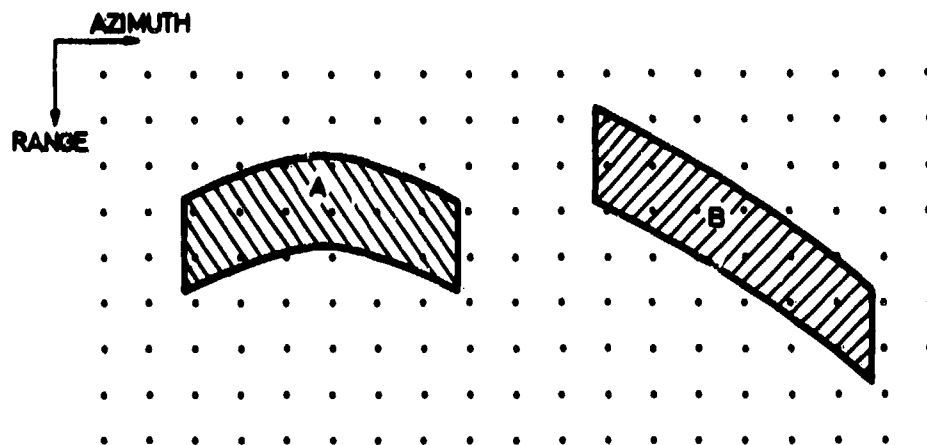
Figure 4.1   Twodimensional digital data format

The dots represent the recorded samples, i e one
vertical line represents one sampled pulse echo.
The area A shows how the echo from a single target
is distributed in the recorded data when the radar
antenna is pointing directly normal to the direction
of relative motion between target and antenna. The
distribution of the target history in range is
caused by the length of the transmitted pulse, and
the distribution in azimuth represents the synthetic
aperture.

B is the target history for a squinted system and
represents the typical target history with SEASAT-1.

The processing of a SAR-image from rawdata means
to compress the target history in both range and
azimuth to an extension equal to approximately one
sample in both directions.

While the range compression is strictly onedimensional
and, as shown in section 3.1, completely azimuth
independent, the azimuth history is curved in the
range direction, socalled range migration, and it
is also range dependent. In the next two sections
range and azimuth compression will be treated separately.

A block diagram of the processor is shown in figure
4.2.

Figure 4.2 Block diagram of digital processor

After a suitable block of rawdata has been written to
disc, the doppler centroid in the azimuth spectrum is
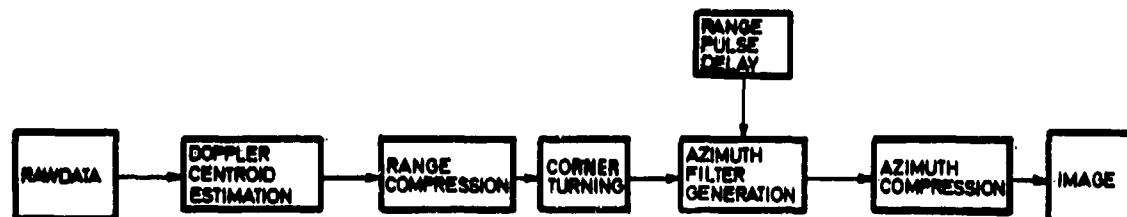estimated. The estimation algorithm is very imple
and it is briefly explained in Appendix A. When the
doppler centroid is estimated, a block of rawdata is
compressed in range, and an interpolation is performed
for each range compressed vector before it is written
back to disc.

Since disc is a onedimensional storage medium, the
range compressed datablock has to be transposed, or
corner turned, before it can be accessed in the
azimuth direction. This corner turning is done
effectively by means of the socalled Eklundh's
algorithm. It is explained in (13). After corner
turning the azimuth filters are generated. To
generate the correct matched filters for azimuth
compression, three parameters related to the satellite
orbit and attitude are needed. These are

1) distance between radar and target
2) effective squint angle of the system
3) relative velocity between antenna and target

The two last parameters will be treated in more detail
later, but briefly it can be said that 1) is given
by the parameter called range pulse delay in figure
4.2, 2) is given by the doppler centroid in the
azimuth spectrum, and 3) is estimated by the auto-
focusing procedure described in section 4.4.

During azimuth compression the four looks are
separately generated and afterwards incoherently
added to give the final multi-look image.

To generate a complete image the sequence of processing
steps is repeated a number of times except the doppler
centroid estimation and the generation of the azimuth
filters.

The theory of linear digital filtering is described
in (14). Digital filtering can be done either in
the time or frequency domain, where frequency domain
filtering is more efficient, measured in number of
operations, for filter lengths more than approximately
30 samples. Since the lengths of the matched filters

used here are typically several hundred samples, the
pulse compressions are done in the frequency domain.
Forward and inverse digital Fourier transforms (DFT)
are calculated by means of the Fast Fourier Transform
algorithm (FFT), described in (15).

The theory of matched filtering can be found in (5).

The details of the algorithms will depend on the
radar system used and the actual system parameters.
There will for example be operations that are
necessary when processing data from a satellite
borne synthetic aperture radar that would not be
necessary if the radar was airborne, and vice versa.
Although the algorithms developed here are for a
satellite borne radar, they include all the principles
of the synthetic aperture radar and could, with some
modifications, be used also for airborne SAR.

A detailed description of the algorithms developed here
together with computer programs written in FORTRAN that
implement these algorithms on a general purpose computer
are given in (16).

4.2   Range compression

During range compression each pulse echo is filtered
with a filter matched to the transmitted linear FM-
pulse. This corresponds to removing the range distri-
bution of the target history as it is shown in figure
4.2.

The analog to digital conversion of each pulse echo is
done to 5 bit real samples. During range compression
these are converted into complex samples which reduces
the sampling frequency in range with a factor 2. This

also reduces the range migration of the target
histories with a factor 2 measured in number of
samples. This makes the range migration correction
during the azimuth compression easier, and it gives
directly the phase information necessary for generating
the synthetic aperture. The real to complex conversion
is done as follows.

A DFT of a 2N-point real sequence gives a 2N-point
complex sequence where the upper half of the sequence
of frequency components is given as the complex
conjugate of the lower half. By discarding the upper
N complex frequency components and taking an N-point
inverse DFT (IDFT) of the rest of the sequence, an
N-point complex time sequence is obtained which
represents the complex version of the 2N real samples.

Another method for obtaining the complex samples
would be to take the Hilbert transform of the real
samples, which would then give the imaginary parts
of the complex samples.

The transmitted pulse is a linear FM-pulse with chirp-
rate $5.63 \cdot 10^{11}$ Hz/sec. On complex form its duration
is 768 samples, and the frequency spectrum is shown
in figure 4.3.

Figure 4.4 shows the received frequency spectrum
averaged over 100 pulse echoes.

When a suitable block of rawdata has been written to
disc and the doppler centroid has been estimated,
range compression is performed. This pulse compression
is accomplished by filtering one range vector from the
rawdata matrix at a time with a filter matched to the
transmitted pulse, and storing the undistorted output
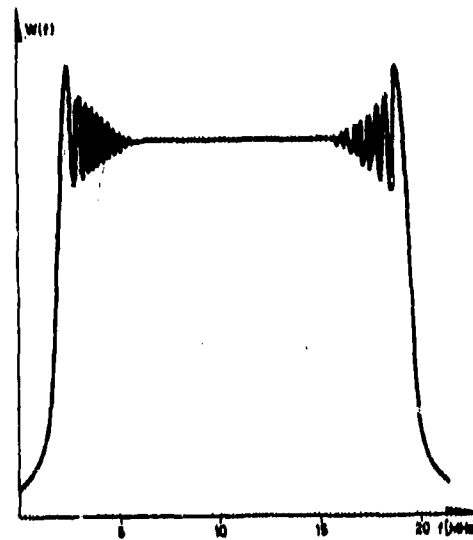values in matrix form on disc.

Figure 4.3 Frequency spectrum of transmitted pulse
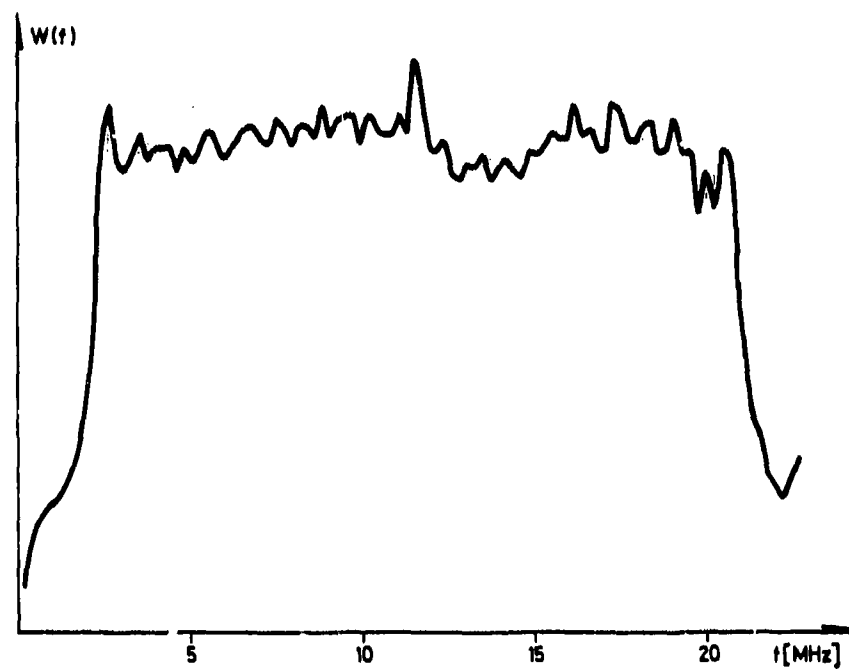
Figure 4.4 Averaged received spectrum in range

The rawdata is packed with three 5 bit samples in a 16 bit word, and the unpacking necessary prior to range compression is done in the same routine that does the range compression.

Conversion from real to complex samples as mentioned above, is efficiently done by utilizing an N-point complex FFT routine for the transformation of 2N real samples, and afterwards descrambling the output values of the FFT routine to get the N complex frequency components wanted. The method is described in (15).

Figure 4.5 shows a block diagram for the range compression routine.
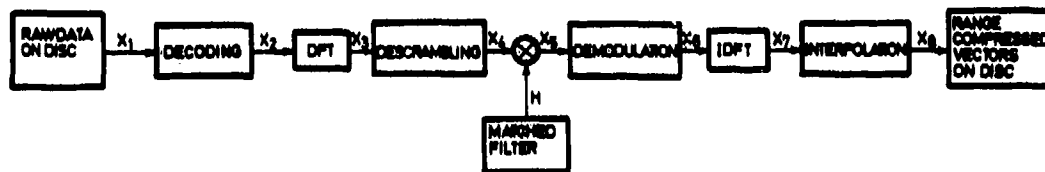
Figure 4.5 Block diagram for range compression

The input vector x_1 contains coded real 5 bit samples. x_1 is decoded to the complex vector $x_2(i)$, $i = 0, N-1$, where $N = 4096$ is a typical length chosen as processing vector length. The consecutive real samples are stored in $Re\{x_2(o)\}$, $Im\{x_2(o)\}$, $Re\{x_2(1)\}$, $Im\{x_2(1)\}$, --. Fourier transformation gives

$$x_3(i) = \sum_{k=o}^{N-1} x_2(k) \cdot exp\{-j\frac{2\pi}{N}i \cdot k\}, \quad i = 0, N-1$$

Descrambling is done according to the following algorithm.

$$\text{Re}\{x_4(i)\} = [\frac{R(i)}{2} + \frac{R(N-i)}{2}] + \cos\frac{\pi i}{N}[\frac{I(i)}{2} + \frac{I(N-i)}{2}]$$

$$- \sin\frac{\pi i}{N}[\frac{R(i)}{2} - \frac{R(N-i)}{2}]$$

$$\text{Im}\{x_4(i)\} = [\frac{I(i)}{2} - \frac{I(N-i)}{2}] - \sin\frac{\pi i}{N}[\frac{I(i)}{2} + \frac{I(N-i)}{2}]$$

$$- \cos\frac{\pi i}{N}[\frac{R(i)}{2} - \frac{R(N-i)}{2}], \quad i = 0, N-1$$

where $R(i) = \text{Re}\{x_3(i)\}$, $I(i) = \text{Im}\{x_3(i)\}$, and $x_3(N) = x_3(o)$

The matched filter's frequency components $H(i)$, $i = 0, N-1$, are calculated and stored before range compression begins. Filter multiplication gives

$$x_5(i) = x_4(i) \cdot H(i), \quad i = 0, N-1$$

The received pulse echoes have a carrier frequency which is half the complex sampling frequency. Demodulation is given as

$$x_6(i) = x_5[(i+\frac{N}{2})\text{modulo } N], \quad i = 0, N-1$$

Transformation back to the time domain

$$x_7(i) = \frac{1}{N} \sum_{k=o}^{N-1} x_6(k) \cdot \exp\{j\frac{2\pi}{N} i \cdot k\}, \quad i = 0, N-1$$

Because of "wrap-around" in the filtering, the undistorted output values are

$$x_7(i), \quad i = 0, M-1$$

where $M = N-767$, since the length of the impulse response of the matched filter is 768 samples.

Interpolation in x_7 uses a 4-point interpolation
filter which gives

$$x_8(i) = \sum_{k=0}^{3} x_7(i+k+m) \cdot \frac{\sin[(k-1-\tau)\pi]}{(k-1-\tau)\pi}, \quad 0 \leq \tau < 1, \quad i = 0, M-4 \quad (4.1)$$

m and τ vary from pulse to pulse and are determined
as explained in section 4.3. The filtered vector
x_8 is then written to disc.

No weighting is applied to the range pulse to reduce
the sidelobe level, and the time response after
compression is shown in figure 3.5. The highest
sidelobes are at -13 dB.

To illustrate the effect of range compression, a
portion of rawdata is shown in figure 4.6 and it
is seen to be completely noiselike. Noise or
interference can be seen on some of the pulse echoes,
but it is suppressed during the processing. Figure
4.7 shows the same data matrix after range compression,
and it is seen that there is considerable structure in
the range direction, while all the features in the
azimuth direction are still smeared out.

4.3 Azimuth compression

After range compression of a suitable block has been
completed, and corner turning is performed, the matrix
has to be compressed in the azimuth direction, i e
filtering rowwise in the data matrix in figure 4.1.

Of the two types of target histories shown in figure
4.1, type A can be regarded as a special case of type
B. After range compression and before interpolation
a typical target history therefore appears as shown in
figure 4.8.

Figure 4.6   Block of rawdata
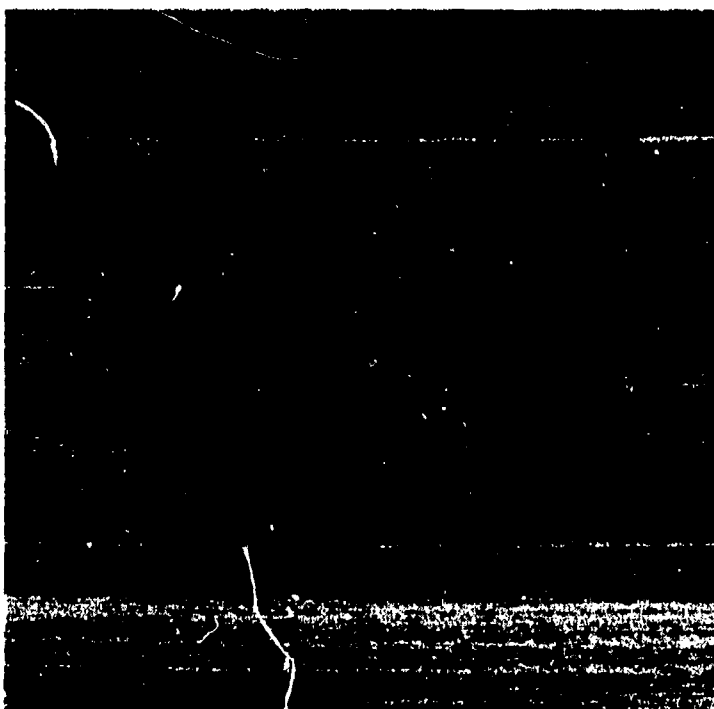
Figure 4.7   Datablock in figure 4.6 compressed in range
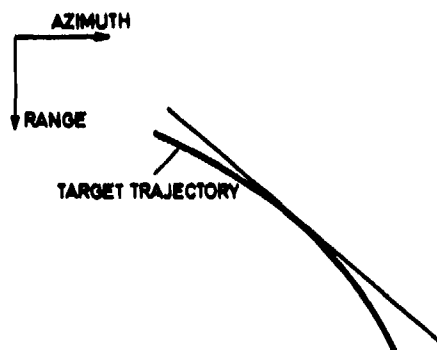
Figure 4.8   Target history after range compression

As described in section 3.2, the recorded target
trajectory is given by

$$r(t) = (R_o^2 + v^2 t^2)^{\frac{1}{2}}, \quad T_1 < t < T_2$$

where T_1 and T_2 determine which part of the hyperbola
by which $r(t)$ is given, is recorded by the system.

The time $(T_1 + T_2)/2$ corresponds approximately to the
center of the antenna beam, and the doppler frequency
of the recorded azimuth history corresponding to this
value of t is called the doppler centroid of the
azimuth spectrum. Case A in figure 4.1 is thus seen
to be the case of 0 doppler centroid.

A squinted system is a system where the doppler centroid
is not equal to 0. Since the radar effectively samples
the azimuth histories with the PRF, it sees all azimuth
frequencies modulo PRF. This ambiguity can be resolved
for example by calculating the variation in doppler
centroid across the swath, since this variation will
depend upon the squint angle of the system. More

effectively, however, the ambiguity is resolved by
making a piece of an image for each possible value
of the doppler centroid. Incorrect values of the
doppler centroid will then give highly degraded
images. It is here assumed that noe such ambiguity
exists since this turns out to be the typical case
when using a satellite borne SAR.

A typical azimuth spectrum for a squinted system is
shown schematically in figure 4.9 and figure 4.10
shows the azimuth spectrum for one data set from
SEASAT-1 averaged over 100 azimuth vectors.
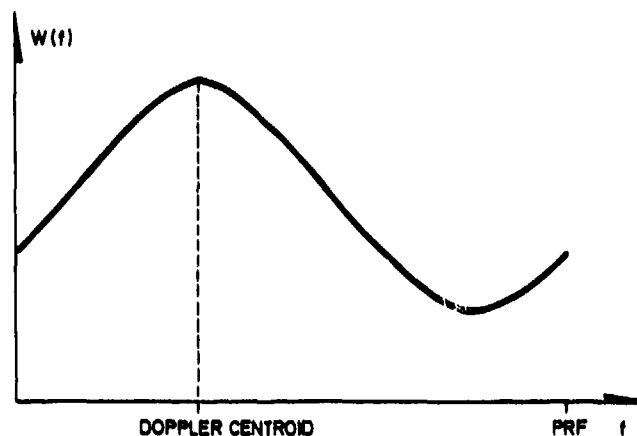
Figure 4.9   Typical azimuth spectrum for a squinted
              system

The range migration of a target is given by the
target's range variation during the observation
interval. Range migration complicates the azimuth
compression, and it should be as small as possible.
The range migration caused by the curvature of the
target trajectory is unavoidable, but for a squinted
system this is small compared to the range migration
caused by the overall inclination of the target
trajectory, as can be seen from figure 4.8. To
minimize range migration the matrix of range compressed
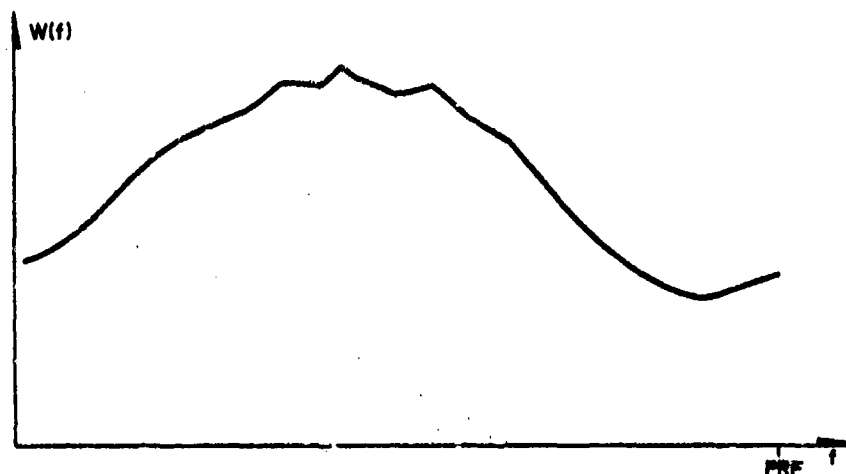
Figure 4.10 Averaged azimuth spectrum from SEASAT-1

data is therefore skewed to make the new azimuth
vectors parallel to the straight line drawn as a
tangent to the target trajectory in figure 4.8. This
is the operation performed by the box termed inter-
polation in figure 4.5, where each range vector is
shifted in range by means of a 4-point interpolation
filter to fit the new azimuth vector direction.

To make the range migration as small as possible, the
new azimuth lines should be tangential to the target
trajectory at the point corresponding to the doppler
centroid. The recorded phase history of a target is

$$\phi(t) = \frac{4\pi}{\lambda} r(t), \quad T_1 < t < T_2$$

The corresponding doppler frequency as a function
of time is

$$f(t) = \frac{1}{2\pi} \frac{d}{dt} [\phi(t)] = \frac{2}{\lambda} \frac{d}{dt} [r(t)]$$

This shows that the inclination of the target trajectory at the point corresponding to a given doppler frequency is directly proportional to this frequency, and does not depend on the actual distance and relative azimuthal velocity between antenna and target.

Since the inclination of the interpolation line is needed prior to range compression, only an estimate of the doppler centroid is needed before range compression begins. This is the reason why the doppler centroid estimation is done directly from the rawdata as shown in figure 4.2.

Typical values for the range migration measured in complex range samples is 100 without interpolation and 8 with interpolation, so the range migration is seen to be considerably reduced by the skewin procedure.

Although the doppler centroid may vary with a couple of hundred Hz across the swath out of an azimuth bandwidth of approximately 1300 Hz, the range migration is still maintained low, even if range migration is minimized only in the middle of the swath. If the whole swath is processed in several blocks, it is possible to use different inclination angles for the interpolation directions for the different blocks, but since the output images are correspondingly skewed, this has to accounted for if the images are mapped together. The images processed here have the same direction of the azimuth lines across the whole swath.

After range compression and skewing a target history looks like shown in figure 4.11.
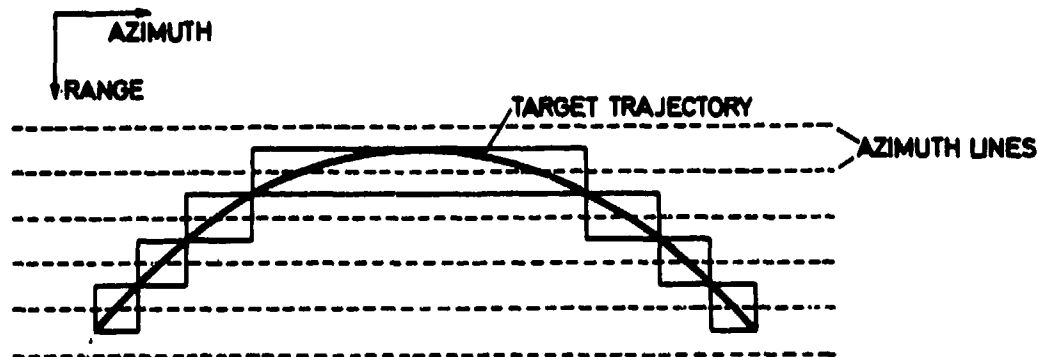
Figure 4.11 Target history after range compression
            and skewing

It is seen that the azimuth history of a single target
is distributed over several azimuth lines. One way to
do the azimuth compression would be to divide the
azimuth filter into several portions as shown by the
seven rectangles in figure 4.11, filter each azimuth
vector with all these filters, and afterwards combine
the outputs in a proper way to get the total azimuth
history compressed. The drawback with this method is,
however, that a number of filters will have to be used
for each azimuth vector, and this is very time consuming.

A method which requires only one azimuth filter is to
do the straightening of the azimuth histories in the
frequency domain. This is explained in figure 4.12,
where F means Fourier transform.

To the left is shown the matrix form of range compressed
data and the trajectories for two targets at the same
range but at different azimuth locations. To the right
is shown the trajectories after Fourier transformation
of the azimuth vectors. The two trajectories are then
seen to coincide. This is because the azimuth histories
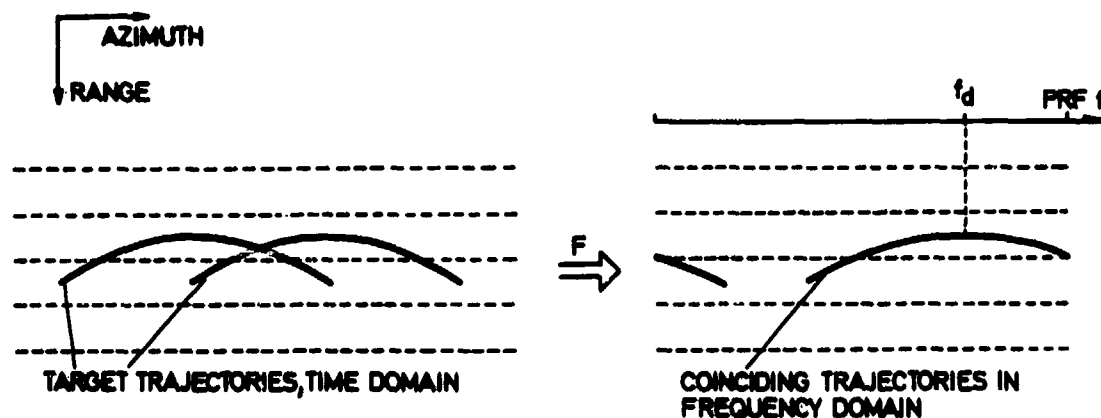
Figure 4.12 Azimuth histories in time and frequency domain

are essentially linear FM-pulses. Because of this
there is a one-to-one correspondence between position
along the azimuth history and instantaneous frequency
of the azimuth history. Said in another way, for a
given azimuth vector the portions of the azimuth
histories of the two targets shown in figure 4.12
that fall within this azimuth vector, contain the
same frequency components. Therefore they will be
mapped together when taking the Fourier transform of
the azimuth vectors. The distinction between different
targets in the frequency domain is represented by the
complex phase factors of the frequency components.

Because of the different values that the doppler
centroid f_d can attain, it is seen from figure 4.12
that in general the azimuth histories will be wrapped
around in the frequency domain.

In the frequency domain it is thus possible to
straighten the trajectories, since this will affect
all targets along an azimuth vector simultaneously,

while a similar straightening in the time domain would
be valid only for a single target.

How well this straightening procedure works, depends
on how accurate the relationship between the time and
frequency domain representations is for a linear FM-
pulse. This again depends on the time-bandwidth
product of the chirppulse. It is seen from figure
4.11 that it is the frequency bands at the ends of the
azimuth history that have the smallest time bandwidth
products. In the case of SEASAT-1 these time bandwidth
products are well above the value necessary to make the
straightening procedure work well. If the skewing
procedure for the range compressed data matrix were not
to be done, this would have made the time-bandwidth
products much smaller than when skewing is applied.

As shown in section 3.2.2 the same azimuth filter can
be used for a range interval of 1105 m if 1 dB
degradation is tolerated. This corresponds to 167
complex range samples. After skewing an azimuth
vector does not any longer represent a single range
cell. With a doppler centroid of 1000 Hz and a
processing block of 4096 samples in azimuth, the
additional range interval is 33 complex samples. To
accommodate different doppler centroid values the
same azimuth filter is therefore used for a block of
100 azimuth vectors for the processing done here.
This gives a total of 61 azimuth filters across the
whole swath. These are calculated and stored before
the azimuth compression begins. Section 4.4 explains
how they are generated.

To reduce the speckle in the images, the azimuth
history is divided into four looks, the output images
of which are added incoherently as explained in
section 3.4. Each look has a duration of 1024 complex

samples and neighboring looks have 1/3 overlap. No
weighting is applied to match the radar antenna
diagram, but to reduce the sidelobe level each look
is weighted with a window function as shown in
figure 4.13. The frequency spectrum of a weighted
look is shown in figure 4.14.

$$w(\tau) = \sqrt{\frac{\sin[(\tau-0.5)\cdot\pi]}{(\tau-0.5)\pi}}$$
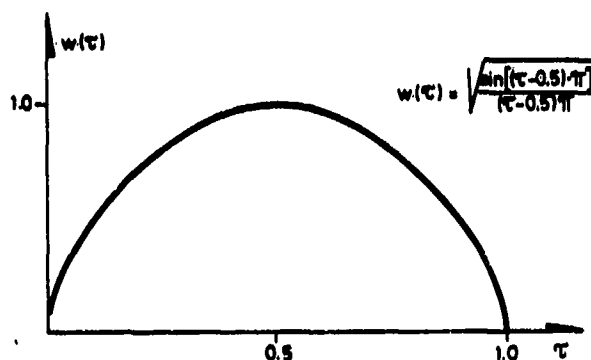
Figure 4.13 Window function applied to each look
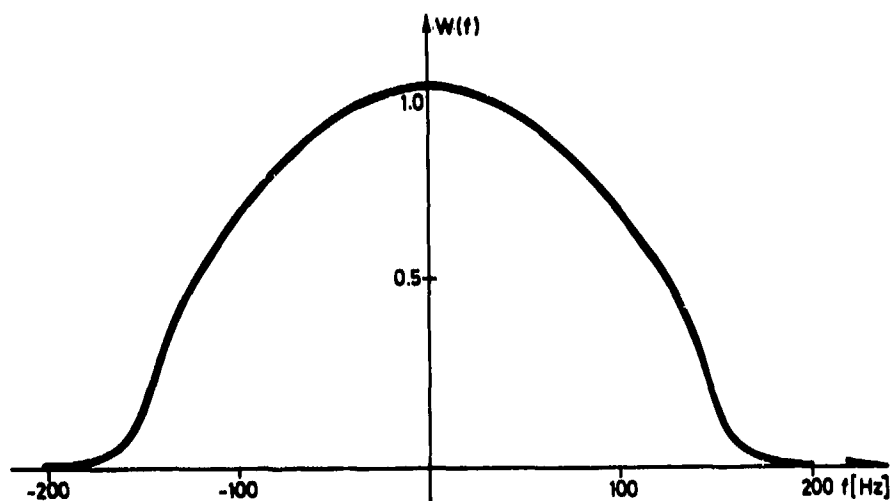
Figure 4.14 Frequency spectrum for one look

The output for one look and a single target is given
in figure 4.15. The sidelobe level is -20 dB, and

the 3 dB width of the peak corresponds typically to
an azimuth resolution of 25 m.
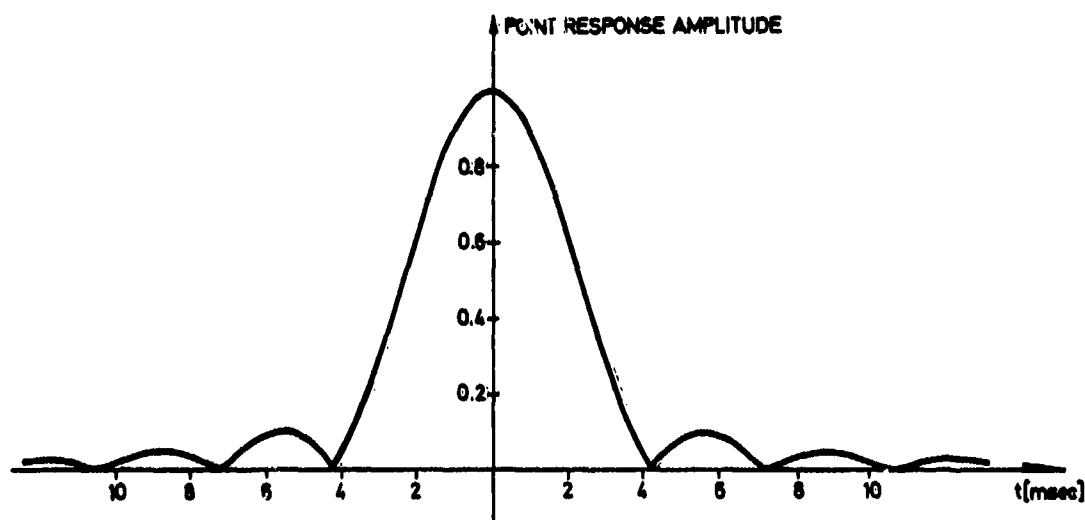
Figure 4.15   Point response of azimuth filter

A block diagram describing the azimuth compression
operation is given in figure 4.16.
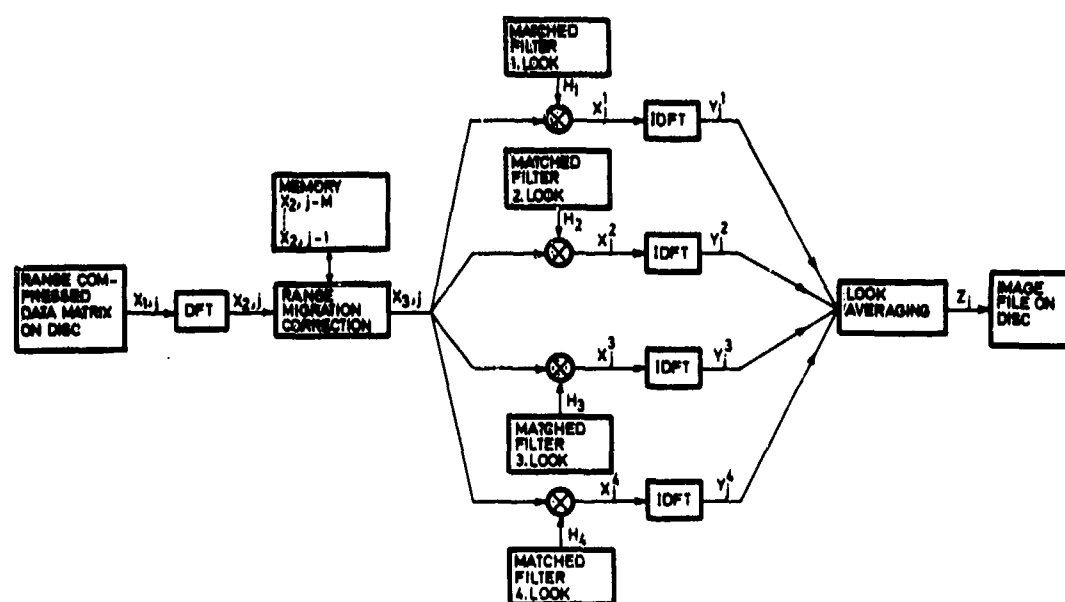
Figure 4.16   Block diagram for azimuth compression

The range compressed data matrix on disc consists of a set of complex azimuth vectors, $x_{1,j}(i)$, $i = 0,N-1$, $j = 0,J-1$, where j is a range index, increasing j meaning increasing range. $N = 4096$ has been used in this work.

Fourier transformation of an azimuth vector gives

$$x_{2,j}(i) = \sum_{k=0}^{N-1} x_{1,j}(k) \cdot \exp\{-j\frac{2\pi}{N}ik\}, \quad i = 0,N-1, \quad j = 0,J-1$$

The range migration correction straightens the azimuth histories as shown in the following. M is chosen such that the number of available transformed azimuth vectors in memory, M+1, is great enough to include the whole trajectory plus a few extra azimuth vectors needed in the interpolation.

The doppler frequency history of a target is

$$f(t) = \frac{1}{2\pi}\frac{d\phi(t)}{dt} = \frac{2}{\lambda}\frac{d}{dt}[(R_o^2+v^2t^2)^{\frac{1}{2}}] = \frac{2v^2}{\lambda}t(R_o^2+v^2t^2)^{-\frac{1}{2}},$$

$$T_1 < t < T_2$$

If the doppler centroid is f_d, the corresponding time $t_d = \frac{1}{2}(T_1+T_2)$ is given by $f(t_d) = f_d$, or

$$t_d = \frac{\lambda f_d R_o}{2v^2}(1-\frac{\lambda^2 f_d^2}{4v^2})^{-\frac{1}{2}}$$

The inclination of the interpolation line used during range compression is

$$\alpha = \frac{d}{dt}r(t)\Big|_{t=t_d} = \frac{\lambda}{2}f(t_d) = \frac{\lambda \cdot f_d}{2}$$

α then determines the values of m and τ in (4.1). The remaining range migration after interpolation in range is

$$\Delta r(t) = r(t) - \alpha \cdot t - [r(t_d) - \alpha \cdot t_d], \quad T_1 < t < T_2$$

If the time-frequency correspondence for a linear FM-pulse is assumed preserved after Fourier transformation, the range migration as a function of frequency is

$$\Delta r(f) = \Delta r[t(f)] = \Delta r[t = \frac{\lambda R_0}{2v^2} f (1 - \frac{\lambda^2 f^2}{4v^2})^{-\frac{1}{2}}]$$

The range migration is then corrected by means of a 4-point interpolation filter in range to fit the curved target trajectory. This is done according to the formula

$$x_{3,j}(i) = \sum_{n=0}^{3} x_{2,j-M+n+K(i)}(i) \cdot \frac{\sin[(n-1-\tau)\pi]}{(n-1-\tau)\pi}, \quad 0 \leq \tau < 1$$

$$i = 0, N-1$$

$$K(i) = [\frac{\Delta r(i)}{\delta_r}]_{int} \quad , \quad \tau = \frac{\Delta r(i) - \delta_r \cdot K(i)}{\delta_r}$$

where $[\ ]_{int}$ means integer part. δ_r is the sample spacing in range measured in meters, and

$$\Delta r(i) = \Delta r(f = \frac{PRF}{N} i)$$

If the actual azimuth frequencies are outside the band [0,PRF], this must be accounted for when $\Delta r(i)$ is calculated.

Referring to figure 4.11, δ_r is the spacing between the azimuth lines, $K(i) = 0$ inside the mid rectangle, increasing with 1 when the trajectory enters a new set of rectangles, and τ measures how close the trajectory is to the upper edge of the rectangle.

The frequency components in $x_{3,j}$ outside the 4 looks are set to zero.

Multiplication with the matched filters for the four looks gives

$$x_j^{\ k}(i) = x_{3,j}[i+\ell(k)] \cdot H_k(i), \quad i = 0, \tfrac{N}{4}-1, \quad k = 1,4$$

where $\ell(k)$ is determined by where in the frequency region $[0,PRF]$ look no. k lies. The index $i+\ell(k)$ is calculated modulo N.

Transformation back to the time domain

$$y_j^{\ k}(i) = \frac{1}{N} \sum_{n=0}^{\frac{N}{4}-1} x_j^{\ k}(n) \cdot \exp\{j\tfrac{2\pi}{N}in\}, \quad i = 0, \tfrac{N}{4}-1, \quad k = 1,4$$

If the number of undistorted output values in $y_j^{\ k}$ is L, and neighboring looks overlap with $4L_1$ samples (with sampling frequency equal to the PRF), $L_1 < \frac{L}{3}$, look averaging gives

$$\begin{cases} |y_j^{\ 1}(i)|^2 & , \ 0 \leq i \leq L_1 - 1 \\[2mm] |y_j^{\ 1}(i)|^2 + |y_j^{\ 2}(i)|^2 & , \ L_1 \leq i \leq 2L_1 - 1 \\[2mm] |y_j^{\ 1}(i)|^2 + |y_j^{\ 2}(i)|^2 + |y_j^{\ 3}(i)|^2 & , \ 2L_1 \leq i \leq 3L_1 - 1 \end{cases}$$

$$z_j(i) = \begin{cases} |y_j^1(i)|^2 + |y_j^2(i)|^2 + |y_j^3(i)|^2 + |y_j^4(i)|^2, & 3L_1 \leq i \leq L-1 \\[2ex] |y_j^2(i)|^2 + |y_j^3(i)|^2 + |y_j^4(i)|^2, & L \leq i \leq L+L_1-1 \\[2ex] |y_j^3(i)|^2 + |y_j^4(i)|^2, & L+L_1 \leq i \leq L+2L_1-1 \\[2ex] |y_j^4(i)|^2, & L+2L_1 \leq i \leq L+3L_1-1 \end{cases}$$

The corresponding azimuth vector from the previously processed block for the same range interval but a different azimuth interval is read from disc and z_j is added to this vector at the correct azimuth position and it is written back to disc. The image file on disc therefore always contains an image that is tapered in number of looks towards the end in the azimuth direction.

In section 4.2 an example of a rawdata image and the corresponding image after range compression was given. In figure 4.17 the range compressed image is repeated for comparison purposes, and the corresponding image after azimuth compression is shown in figure 4.18. The fully processed image has a resolution of 25mx25m and contains 4 looks. To make the fully processed image requires 7 times as much range compressed data in the azimuth direction as is shown in figure 4.1, but the relationship between the range compressed image and the mid section of the fully processed image can be seen.

Several examples of images processed to 25mx25m resolution and 4 looks are shown in figures 4.19-4.23.

It was earlier found that the signal to noise ratio for an average sea model after fully coherent processing is 15 dB. This is also the signal to noise ratio after
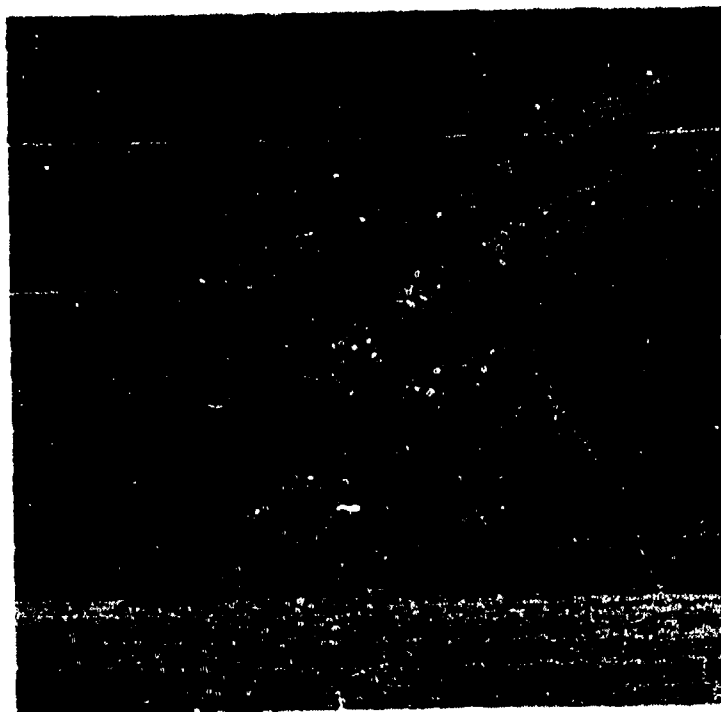
Figure 4.17   Range compressed data block

Figure 4.18   Datablock in figure 4.17 compressed in azimuth to 4 looks

azimuth

Oslofjorden, scale 1:330000
25mx25m resolution, 4 looks

Figure 4.19   Example of digitally processed SAR image

azimuth

Strait of Dover, Dunkirque, scale 1:330000
25mx25m resolution, 4 looks

Figure 4.20   Example of digitally processed SAR image
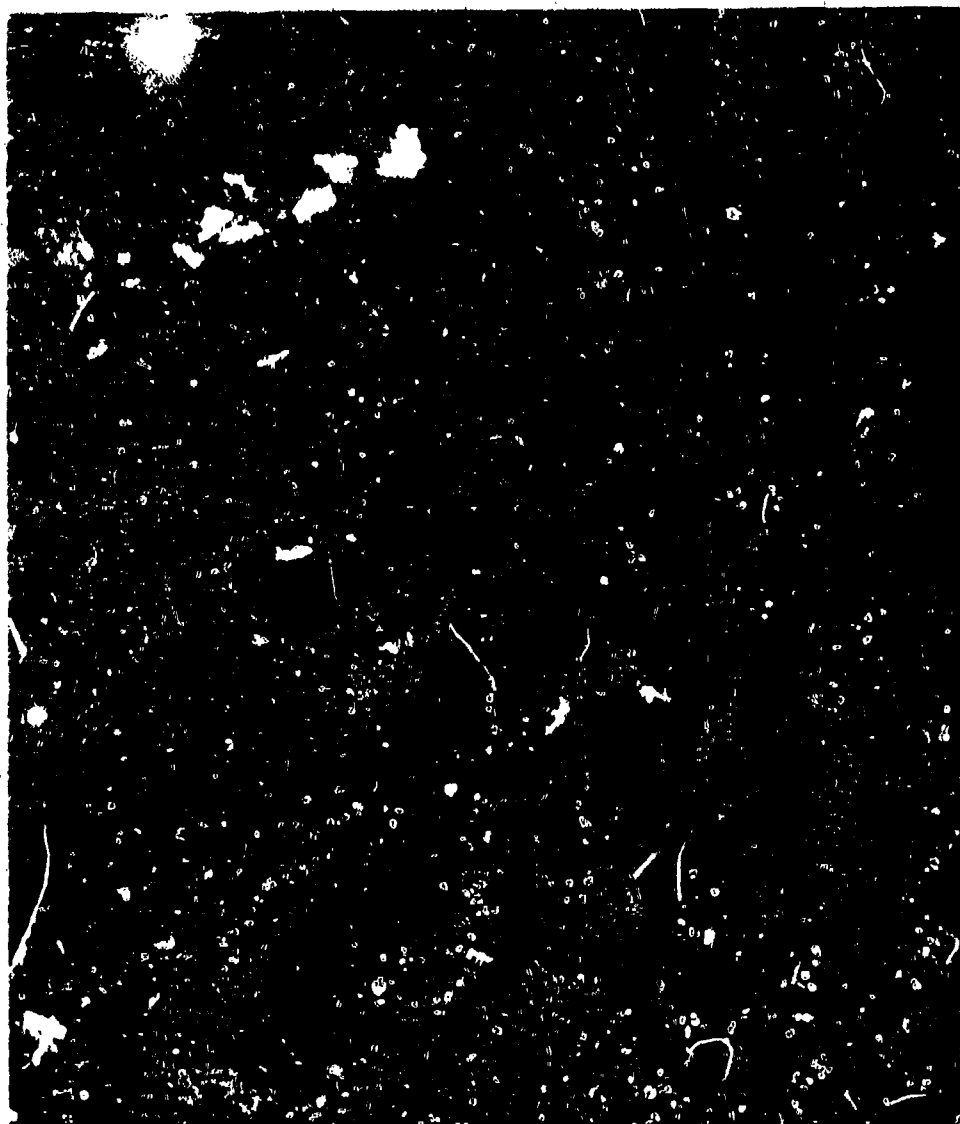
azimuth

Århus, Denmark, scale 1:330000
25mx25m resolution, 4 looks

Figure).21 Example of digitally processed SAR image

azimuth

Sunnfjord, scale 1:330000
25mx25m resolution, 4 looks

Figure 4.22   Example of digitally processed SAR image

azimuth

Fredrikstad, scale 1:330000
25mx25m resolution, 4 looks

Figure 4.23 Example of digitally processed SAR image

1 bit input
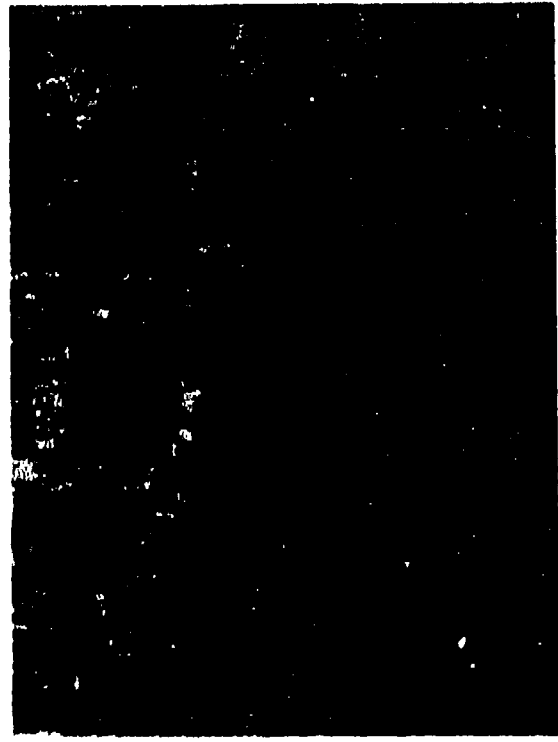
2 bit input
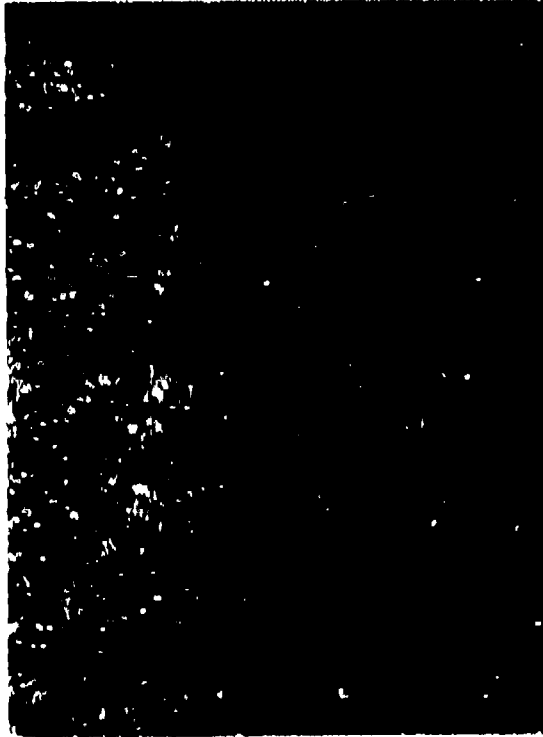
3 bit input

4 bit input

Figure 4.24   Effect of accuracy in input data

the receiver for a pulse echo. Quantization on amplitude
basis requires $\frac{15}{6}\frac{dB}{dB}+1$ signbit $\approx$ 3.5 bits. Figure 4.24
shows an image processed in 4 looks with different
numbers of bits in the input signal. The same image
with 5 bit input is the 4 look image in figure 3.23.
Although the quantization with so few bits cannot be
regarded as introducing additive noise, the high
compression ratio tends to make the effect similar to
the effect of additive noise, as can be seen from
figure 4.24. It can also be seen that the estimate
of 3.5 bits in the input to avoid quantization effects
is quite good. Because of additional noise introduced,
quantization to for example 1 bit to simplify processing
might seriously degrade performance of the target
detection procedure developed in chapter 5.

4.4 Autofocusing for generation of azimuth filters

Before the azimuth processing can be done, one has to
have an estimate of the doppler centroid and of the
relative velocity between the targets and the radar
platform. The doppler centroid is estimated before
the range processing, so only the relative velocity v,
which determines the chirprate of the azimuth history,
remains to be estimated.

When v is known, the azimuth history is known as a
function of range. The matched filters for the 4
looks are then generated in the time domain by multi-
plying the azimuth history with the window function
shown in figure 4.13, for 4 different, partially
overlapping sections of the azimuth history, each
1024 complex samples long. The matched filters are
then the complex conjugated Fourier transforms of
the looks' time responses. These matched filters are
all generated and stored before azimuth compression
begins.

One way to estimate v is to calculate it from the orbit
parameters of the satellite. The drawback with this
procedure is, however, that this information has to be
supplied separately from the synthetic aperture radar
data collection itself, and this may take considerable
time. Depending on the time delay, which for SEASAT-1
is on the order of days, this may exclude any operational
use of the data. To avoid this difficulty an auto-
focusing procedure is developed here, which means that
only the data from the synthetic aperture radar is
used to generate an estimate of the relative velocity
v.

The autofocusing is based on maximization of the contrast
in the image. The validity of this criterion can be
seen as follows. If the azimuth compression is done
with an incorrect value of the relative velocity v,
which means wrong chirprate in the azimuth history,
this will result in a smearing of point targets in the
image. This smearing is equivalent to a reduction in
contrast. It is therefore assumed that maximum contrast
occurs for the correct value of v.

The greater the azimuth bandwidth used in the compression,
the more sensitive the contrast is to changes in v.
Compression to 4 looks is therefore used also for the
contrast calculation. This has the advantage that the
routine used for azimuth compression of the whole image
also can be used here.

The contrast C in an image is defined by (3.4), or
equivalently

$$C = \frac{[<I^2>-<I>^2]^{\frac{1}{2}}}{<I>}$$

where I is the intensity and <> denotes expectation.

The estimate for v is obtained by calculating the
contrast curve $C(v)$, i e contrast as a function of
v, for a suitable image area and choosing the value
of v that corresponds to the peak in the contrast
curve. To get a reliable estimate for v, the area
used for calculation of the contrast contains several
thousand image points.

The contrast will be higher and the peak more pronounced
for scenes containing strong specular points than for
scenes with little or no strong point scatterers.
Scenes characterized by fully developed speckle, where
there are many weak specular scatterers inside a
single resolution cell, should not be expected to
show any pronounced peak in the contrast curve because
the intensity distribution in this case, given in
section 3.4, does not depend on focusing of the image.

Figure 4.25 shows four contrast curves obtained
experimentally from one image. The two curves in
the middle are from neighboring, nonoverlapping land
areas. One of the areas is seen to have higher
contrast than the other one, and the peak is more
pronounced. The peaks occur, however, for the same
value of v for both areas, as was expected.

The lowest curve is for a homogeneous sea area. As
shown in section 3.4, such an area is very well
described by fully developed speckle. According to
what was said above, this should not be an area
suitable for focusing, and the contrast curve is
indeed seen to be flat and close to the theoretical
value of 0.5 for a four-look image.

Contrast curves for sea areas that have a pronounced
structure have not been calculated and conclusions
about focusing properties of such areas therefore
cannot be drawn.
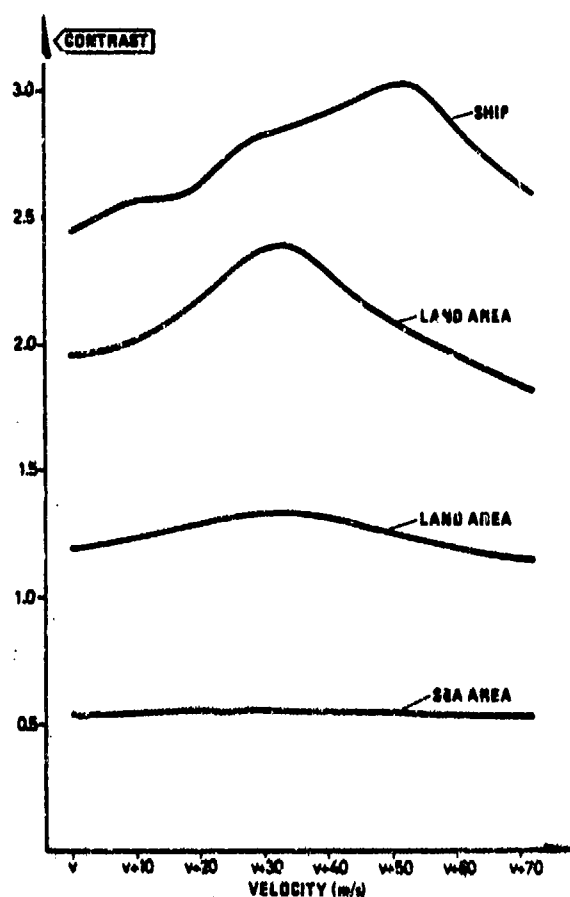
Figure 4.25   Experimental contrast curves

The uppermost curve in figure 4.25 is for a strong
ship target. An autofocusing procedure based on
such targets is not likely to be feasible, since it
would require that the target was detected before
focusing, and since it generally will be moving and
therefore give a wrong estimate for v for generation
of the whole image. It might, however, be possible to
use the method to get an estimate of the targets
azimuthal velocity. If the range component could
be estimated for example from the ship's displacement
from the wake, the total velocity vector could be
estimated.

The ship is moving in the azimuth direction, but in
the opposite direction of the satellite, and the
peak in the contrast curve should therefore be
expected to occur for a somewhat higher velocity than
for the land areas. The curve is, however, seen not to
have the same regular shape as for the land areas, and
the peak corresponds to a target velocity between 35 and
40 knots, which is not likely to be true. Some kind of
mean value obtained from the contrast curve might give
a reasonable velocity, but no good justification for
such a procedure is seen. What can be observed,
however, is that the contrast curve is displaced in
the correct direction relative to the curves for land
areas. This curve is also necessarily calculated for
considerably fewer image points than for the land areas,
and the statistical properties therefore cannot be
expected to be very good.

The autofocusing procedure has been tried for many
cases and has been found to work well for land areas.
When imaging coastal areas, the land areas can therefore
be used for focusing which then also will be valid for
the sea areas. By using a precise model for the
satellite's orbital motion it might be possible to
maintain correct focus setting during long passages
over sea areas by updating the orbit parameters during
passages over land.

A suitable search algorithm will make it necessary to
calculate only relatively few points on the contrast
curve before the estimation procedure converges, thereby
minimizing the computational burden imposed by the
autofocusing.

5   TARGET DETECTION IN IMAGES

The ultimate goal when using synthetic aperture radar in
maritime surveillance is not the images as such, but
rather a detection of targets together with an
indication of the targets' positions. When the
targets are ships, they are approximately point targets.
The detection procedure chosen is therefore maximization
of the signal to noise ratio for each point. This leads
to matched filtering where the filter is matched to the
point target response. This is the processor developed
earlier in this work, and the output can be interpreted
as images. Target detection is then done in the images
on an intensity basis.

The method of addition of different statistically
independent looks was used to reduce the speckle in
the images. This was done because it has a positive
effect when the images are regarded by the human eye,
and it also gives a better radiometric resolution,
but it is not necessarily advantageous when applying
an automatic detection procedure to the images. The
effect of look addition is considered below.

The detection of ships in images can be done in several
ways. One method is to let a human operator perform
visual detection in processed images. Figures 3.14,
3.15 and 4.19-4.23 show several examples illustrating
that this is fully possible.

This detection operation should not be done from
photographs because of the poor dynamic range of
intensity in photographic paper. Use of photographs
would also incur an extra time delay which for
operational purposes would be highly undesirable.
In general it can be said that a photographic
reproduction of a synthetic aperture radar image

that is scaled to give a pleasant view of land areas
will, depending on sea state among other things,
highly suppress strong point targets such as ships
because of the poor dynamic range in photographs.

It is seen from the examples mentioned that an interesting
way of detecting moving ships is by detection of the wake
of the ship rather than of the ship itself, or both.
With a human operator this is easily achieved.

While the detection of ships in images by means of
the ship itself, or its wake, is easily combined
in the case of a human operator, these two methods
of target detection are completely different in the
case of automatic target detection. A method based
on detection of wakes in an image would be a pattern
recognition technique, and this is not considered
here. Besides, a wake is a distributed phenomenon,
the detection of which might be done more optimally
than by pattern recognition in an image. Another
method might be less time consuming than full processing
of images, and this would be very important in the
case of operational use.

As mentioned above, the detection procedure developed
here is based on the target's intensity in the image.
In statistical terms this problem is called the binary
hypothesis testing problem, (17). If I is the
intensity in a given image point, s is the intensity
caused by a target and n is the intensity of the sea,
we have to test I against the following two hypotheses

H_1: $I = s+n$
H_0: $I = n$

If H_1 is true, the point is a combination of a target
and the sea, and if H_0 is true, there is no target in

the point. Depending on the size of the target and
how much of the image point that is occupied by the
target, an alternative set of hypotheses could be

$$H_1': \quad I = s$$
$$H_0': \quad I = n$$

In this case we have either a target or the sea in
each image point and never a combination of both.
Both sets of hypotheses will be treated.

The two most used test criterions are the ones due to
Bayes and Neyman-Pearson, (17). The Bayesian
approach requires a priori probabilities of there
being a target or not and an assignment of costs
to the four different combinations of two outcomes
and true and false hypothesis. Because of the problems
in assigning reasonable values to both, the Neyman-
Pearson criterion is usually applied in radar detection
problems.

When the Neyman-Pearson test is used, only two of the
four possible combinations of outcomes and input
hypotheses are used. These are the probability of
detection, P_D, which is the probability of saying that
H_1 is true when it is true, and the probability of
false alarm, P_F, which is the probability of saying
that H_1 is true when H_0 is true. The criterion used
is to maximize P_D subject to the constraint $P_F \leq \alpha$,
i e the probability of detection is maximized while
the probability of false alarm is kept below a certain
threshold. This method thus emphasizes the importance
of not giving false alarms.

It can be shown, (17) and (18), that both the Bayes
criterion and the Neyman-Pearson criterion lead to a
likelihood ratio test. The likelihood ratio is
defined as

$$\ell(I) = \frac{p(I|H_1)}{p(I|H_0)}$$

that is the ratio between the conditional probabilities of the cbserved intensity given H_1 and H_0, respectively. The decision algorithm is then

If $\ell(I) \geq n$,   say H_1 is true

If $\ell(I) < n$,   say H_0 is true

The value of the threshold n depends on the values chosen for P_D and P_F. The detector is thus a processor that generates the likelihood ratio $\ell(I)$ for each image point and decides which hypothesis is true by comparing $\ell(I)$ with the threshold n.

To find the performance of the detector it is necessary to calculate the likelihood ratio $\ell(I)$ and the socalled receiver operating characteristics, curves of P_D versus P_F, for the different cases. We thus need the probability distributions for the intensity subject to the two hypotheses, and for different cases such as different numbers of looks.

The probability distribution for the intensity in a onelook image of a sea area is supposed to be given by the probability distribution for fully developed speckle. This distribution was given in section 3.4, and if it is normalized by setting $I_0 = 1$, we get

$p_1(I|H_0) = \exp\{-I\}$, $I \geq 0$ and zero elsewhere.

The subscript indicates the number of looks. The addition of several looks is equivalent to the addition of several independent, identically distributed stochastic variables. The resulting probability distribution is then the convolution of the individual distributions. This is most eusily accomplished

mathematically by applying the moment generating function which is defined by

$$M(s) = \int_{-\infty}^{\infty} p(x) \cdot \exp\{-sx\} dx$$

where $p(x)$ is the probability distribution. The moment generating function for a sum of independent stochastic variables is the product of the individual moment generating functions. Since we here always have $p(x) = 0$, $x < 0$, the moment generating function is equal to the onesided Laplace transform of $p(x)$. We thus get

$$M_1(s) = \int_0^{\infty} p_1(I|H_0) \exp\{-sI\} dI = \int_0^{\infty} \exp\{-(s+1)I\} dI = (s+1)^{-1}$$

The moment generating function for n looks is

$$M_n(s) = (s+1)^{-n}$$

Inverse Laplace transformation gives

$$p_n(I|H_0) = \frac{1}{\Gamma(n)} I^{n-1} \cdot \exp\{-I\}, \quad n \geq 1, \quad <I> = n$$

where $\Gamma(n)$ is the gamma function.

Since we have $H_0 = H_0'$, we also have $p_n(I|H_0) = p_n(I|H_0')$

To find $p_n(I|H_1)$ and $p_n(I|H_1')$ we must know the probability distribution of s, i e the target's intensity distribution. Because of the inherent difficulties in defining this distribution, the most reasonable probability distribution is assumed to be a uniform distribution. We thus have

$$p(s) = \frac{1}{S_o}, \quad 0 \le s \le S_o$$

The significance of the choice of S_o will be commented upon later.

When adding looks, the targets' intensitites and the intensity of the sea background will be statistically independent, and the distribution $p(I|H_1) = p(I|s+n)$ is the convolution of the probability distributions for target intensity and sea intensity. When processing images it has turned out, however, that there is strong interdependence between different looks for strong targets. This is not unexpected since a strong target may consist of perhaps only a single strong reflecting point. The intensity distribution for a target after look addition is therefore not obtained by convolution of the single look distribution with itself several times, but is better modelled by a uniform distribution even after look addition, properly scaled according to the new mean value.

By scaling all the speckle distribution functions to have mean values equal to 1, we get the following distributions.

$$p_n(I|H_0) = p_n(I|H_0') = \frac{n^n}{\Gamma(n)} \cdot I^{n-1} \cdot \exp\{-nI\}, \quad I \ge 0$$

$$p_n(I|H_1') = \frac{1}{S_o}, \quad 0 \le s \le S_o$$

The distribution $p_n(I|H_1)$ is given by the convolution of $p_n(I|H_0)$ and $p_n(I|H_1')$.

$$p_n(I|H_1) = \frac{1}{S_o} \int_0^I p_n(x|H_0)dx = \frac{n^n}{S_0 \Gamma(n)} \int_0^I x^{n-1} \cdot \exp\{-nx\}dx$$

$$= \frac{1}{S_o}[1-\exp\{-nI\} \sum_{m=0}^{n-1} \frac{(nI)^m}{m!}], \quad 0 \le I \le S_o$$

The tail of the distribution $p_n(I|H_1)$ for $I>S_o$ is not calculated since it is not needed.

The likelihood ratios can now be calculated

$$\ell_n(I) = \frac{p_n(I|H_1)}{p_n(I|H_0)} = \frac{\Gamma(n)}{S_o \cdot n^n} \cdot I^{-(n-1)} [\exp\{nI\} - \sum_{m=o}^{n-1} \frac{(nI)^m}{m!}]$$

$$0 \le I \le S_o$$

$$\ell_n'(I) = \frac{p_n(I|H_1')}{p_n(I|H_0')} = \frac{\Gamma(n)}{S_o \cdot n^n} \cdot I^{-(n-1)} \cdot \exp\{nI\}, \quad 0 \le I \le S_o$$

Since

$$\exp\{nI\} = \sum_{m=o}^{\infty} \frac{(nI)^m}{m!}$$

we have

$$\ell_n(I) = \frac{\Gamma(n)}{S_o \cdot n^n} \cdot I^{-(n-1)} \cdot \sum_{m=n}^{\infty} \frac{(nI)^m}{m!} = \frac{\Gamma(n)}{S_o \cdot n} \cdot \sum_{m=n}^{\infty} \frac{(nI)^{m-n+1}}{m!}$$

We therefore have $\frac{d}{dI}[\ell_n(I)]>0$ for $0<I<S_o$ while for $\ell_n'(I)$ we have $\frac{d}{dI}[\ell_n'(I)]<0$ for $0<I<1-\frac{1}{n}$ and $\frac{d}{dI}[\ell_n'(I)]>0$ for $1-\frac{1}{n}<I<S_o$. Also $\ell_n'(I)\to\infty$ when $I\to 0$. This means that $\ell_n'(I)$ cannot be used for the interval $0<I<1-\frac{1}{n}$. The detector will therefore operate as follows for the different intensity intervals.

Hypotheses H_0 and H_1:

$0 \le I \le S_o$: H_0 true if $\ell_n(I)<\eta$

            H_1 true if $\ell_n(I) \ge \eta$

$I>S_o$: H_1 true

Hypotheses H_0' and H_1':

$0 \leq I \leq 1 - \frac{1}{n}$: H_0' true

$I - \frac{1}{n} < I \leq S_o$: H_0' true if $\ell_n'(I) < \eta$

H_1' true if $\ell_n'(I) \geq \eta$

$I > S_0$: H_1' true

η is the decision threshold.

To find the receiver operating characteristics it is necessary to calculate the probability of detection P_D and the probability of false alarm P_F as a function of the intensity threshold γ and the number of looks n. With $\ell(\gamma) = \eta$ or $\ell'(\gamma) = \eta$ we have

$$P_D = \int_\gamma^\infty p_n(I|H_1)dI$$

$$P_F = \int_\gamma^\infty p_n(I|H_0)dI$$

and correspondingly for the primed case.

$$P_D = \int_\gamma^\infty p_n(I|H_1)dI = 1 - \int_0^\gamma p_n(I|H_1)dI$$

$$= 1 - \int_0^\gamma \frac{1}{S_o}[1 - \exp\{-nI\} \sum_{m=0}^{n-1} \frac{(nI)^m}{m!}]dI$$

$$= 1 - \frac{\gamma}{S_o} + \frac{1}{S_o} \sum_{m=0}^{n-1} \frac{n^m}{m!} \int_0^\gamma I^m \cdot \exp\{-nI\}dI$$

$$= 1 - \frac{\gamma - 1}{S_o} - \frac{1}{2 S_o} \exp\{-n\gamma\} \sum_{m=0}^{n-1} \sum_{k=0}^{m} \frac{(n\gamma)^k}{k!}, \quad 0 \leq \gamma \leq S_o$$

$$P_D' = \int_\gamma^\infty p_n(I|H_1')dI = 1 - \frac{\gamma}{S_o}, \quad 1 - \frac{1}{n} \leq \gamma \leq S_o$$

$$P_F = P_F' = \int_\gamma^\infty P_n(I|H_o)\,dI = \frac{n^n}{\Gamma(n)} \int_\gamma^\infty I^{n-1} \cdot \exp\{-nI\}\,dI$$

$$= \frac{n^n}{\Gamma(n)} \cdot \exp\{-n\gamma\} \sum_{k=0}^{n-1} \frac{(n-1)!}{k!} \cdot \frac{\gamma^k}{n^{n-k}}$$

$$= \exp\{-n\gamma\} \sum_{k=0}^{n-1} \frac{(n\gamma)^k}{k!}, \quad \gamma \geq 0$$

The probability of detection P_D is seen to depend strongly upon S_o, which means that a somewhat arbitrary choice of S_o will have considerable effect upon the resulting probability of detection. Since one can write

$$P_D = 1 - \frac{1}{S_o} \cdot f(\gamma, n)$$

where $f(\gamma, n)$ is a function of γ and n, the dependence of P_D upon n, the number of looks, can be found by studying $f(\gamma, n)$ which does not depend on S_o.

The reason why the number of looks n is an important parameter with regard to target detection is the relationship between the coherence time of a target and the coherent integration time in the processor. By coherence time of a target is meant the longest observation time during which the target response can be regarded as coherent. The peak response for a target will increase more strongly for an increase in coherent integration time when this integration time is shorter than the target's coherence time than when it is longer. The coherence time of the sea background, regarded as speckle noise, is of no importance in this case since the speckle distribution functions are independent of coherence time. Since the length of the synthetic aperture is fixed, there is a compromise between coherent integration time (integration time per look) and number of looks.

When comparing the receiver operating characteristics
for different numbers of looks, this must be done with
the same amount of input information in each case to
get relevant results. This means that the total inte-
gration time used for a given number of looks must be
the same for all cases compared. This total integration
time, given by the length of the whole synthetic aperture,
is assumed constant for all cases considered.

The formulas developed above are all derived by means
of speckle distributions which have an expected value
of 1. This represents an intensity scaling. S_o is also
the same in all the formulas.

As a parameter in the comparison of different cases a
coherence factor k_c will be introduced. This factor is
defined below.

If the case of a single look, i e n = 1, is described
by an expected speckle intensity of 1 and a target
intensity distribution that is uniform on the interval
$0 \leq I \leq S_o$, the case of n looks can be described by an
expected speckle intensity of 1 and a target intensity
distribution that is uniform on the interval $0 \leq I \leq k_c S_o$.
We will always have $\frac{1}{n} \leq k_c \leq 1$, where a high value of
target coherence time relative to the coherent integration
time in the processor corresponds to a low value of k_c.
This can be seen as follows.

Given an image which contains n looks. If the coherent
integration time is increased to the case of one look,
the peak intensity of the target relative to the sea in the
onelook image will change from the case of n looks
depending on the coherence properties of the target.
As mentioned above the speckle distribution is independent
of sea coherence time, and the mean value of the speckle
intensity is proportional to the bandwidth of the chirp-
filter when the input speckle noise is considered white

in the frequency band of interest. Mean speckle
intensity is therefore proportional to coherent inte-
gration time. If the target is coherent over the
whole observation time, an increase in coherent inte-
gration time with a factor n will result in a peak
intensity increase for the target with a factor n^2.
Since the mean sea intensity increases with a factor
n, this gives $k_c = \frac{1}{n}$. The other extreme case is when
the target coherence time is shorter than the coherent
integration time corresponding to n looks. In this case
target peak intensity increases incoherently, i e
proportionally with coherent integration time, and we
have $k_c = 1$.

Figures 5.1 and 5.2 show the receiver operating
characteristics for $k_c = 1$, $k_c = \frac{1}{n}$ and n = 1,2,3,4.
S_o is chosen 100. Only the primed case is shown since
the unprimed case exhibits the same principal behaviour.

The figures show that in the case of $k_c = 1$, the
maximum number of looks should be chosen, and when
$k_c = \frac{1}{n}$, one look should be chosen. This is intuitively
logical since in the first case there is nothing to be
gained by increasing the coherent integration time, while
averaging of several looks will suppress the upper tail
of the sea intensity distribution, thereby increasing the
detection probability for a given false alarm probability.
Likewise for $k_c = \frac{1}{n}$, the target detection probability is
highest when using a single look.

Since the order of the receiver operating characteristics
in figures 5.1 and 5.2 for different values of n is seen
to be reversed, there is obviously a value of k_c for
which the receiver operating characteristics for two
given numbers of looks are equal for any chosen value
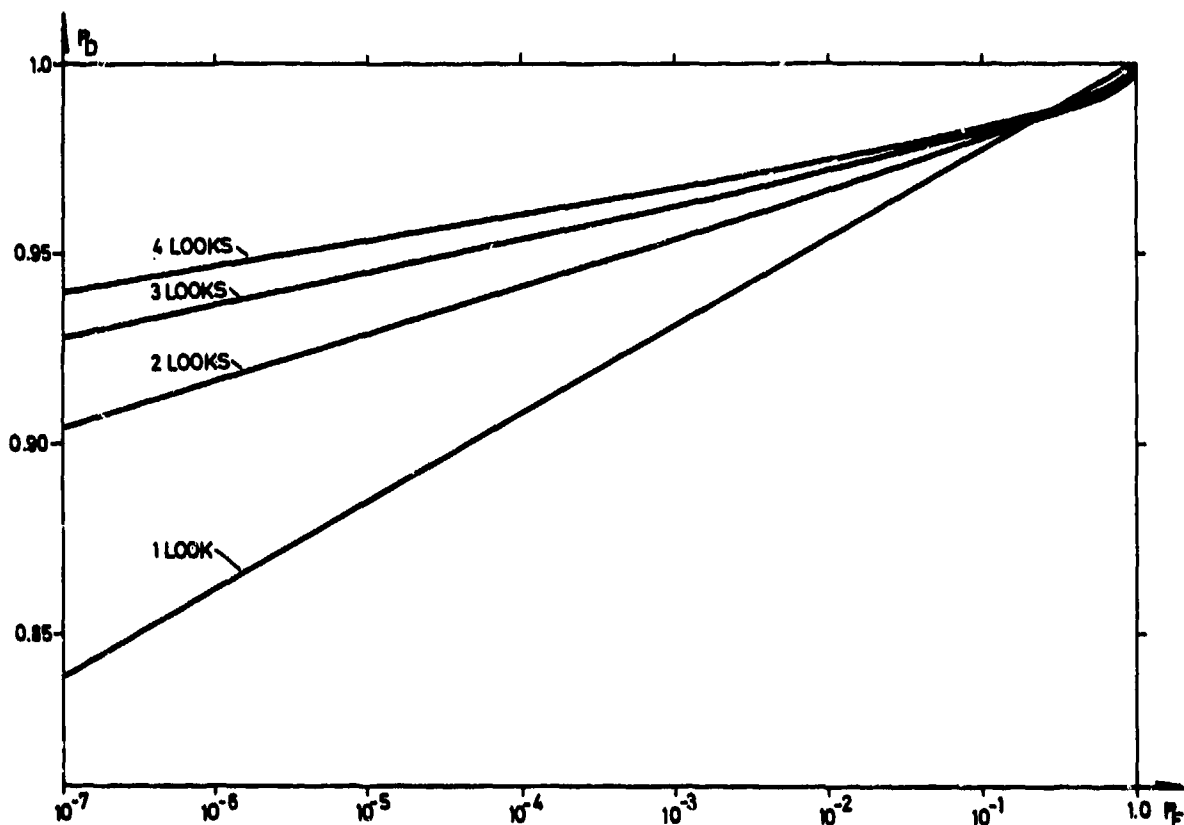of false alarm probability P_F.

Figure 5.1   Receiver operating characteristics with $k_c = 1$

To be able to choose the optimum number of looks, the coherence properties of typical targets must be known. These properties can be expressed by a function that shows how the expected peak intensity of a target changes with coherent integration time, that is integration time per look

If T is the total integration time, i e the length of the azimuth history, then $g(\tau) = \frac{\tau}{T}$ gives the normalized expected intensity of the sea, where τ is the coherent integration time, $0 \leq \tau \leq T$. $f(\tau)$ is the corresponding curve for a target, and it is closely related to the correlation function of the target's azimuth history. $f(\tau)$ can best be obtained empirically. Figure 5.3 shows $g(\tau)$ and a possible normalized $f(\tau)$.
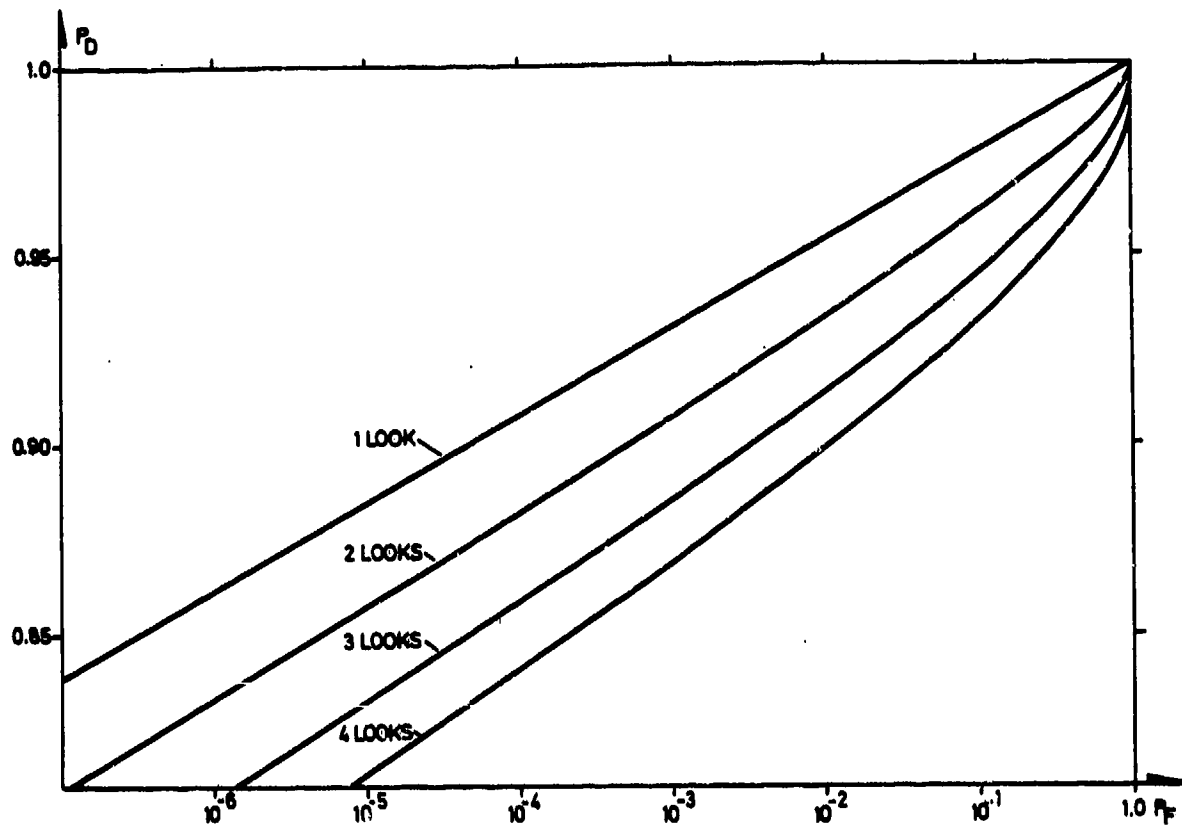
Figure 5.2   Receiver operating characteristics with
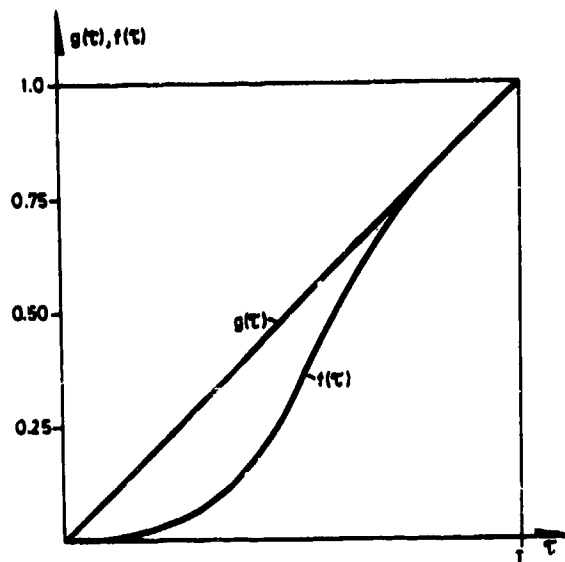$$\underline{k}_c = \frac{1}{n}$$

Figure 5.3   Principal behaviour of expected peak target
intensity and expected mean sea intensity as
functions of coherent integration time

The parabolic portion of $f(\tau)$ gives the integration times for which the target response is highly coherent. The linear portion of $f(\tau)$ represents an incoherent increase in peak intensity as the coherent integration time is increased.

To find the optimum number of looks the receiver operating characteristics must be plotted. The curves $g(\tau)$ and $f(\tau)$ will then determine the coherence factor k_c, which is given as a function of n by the expression

$$k_c(n) = \frac{f(\frac{T}{n})}{g(\frac{T}{n})} = n \cdot f(\frac{T}{n})$$

If the functional form of $f(\tau)$ were known, the optimum number of looks could be calculated. Instead a single case with a ship target has been tried experimentally by processing to 1 and 3 looks, respectively. By comparing the peak intensity of the ship with the mean intensity of the surrounding sea, a coherence factor of 0.59 was found. Figure 5.4 shows the receiver operating characteristics for 1 and 3 looks with $k_c = 0.59$. It is seen from the figure that in this case it is advantageous to use 3 looks if a false alarm rate less than approximately $5 \cdot 10^{-3}$ is desired.

A generalization not considered here is to use overlapping looks. This would give partially correlated looks and the resulting receiver operating characteristics would be somewhat different from the ones derived above.

Since the total integration time is constant, the azimuth resolution will be degraded as the number of looks is increased. Depending on the target size,
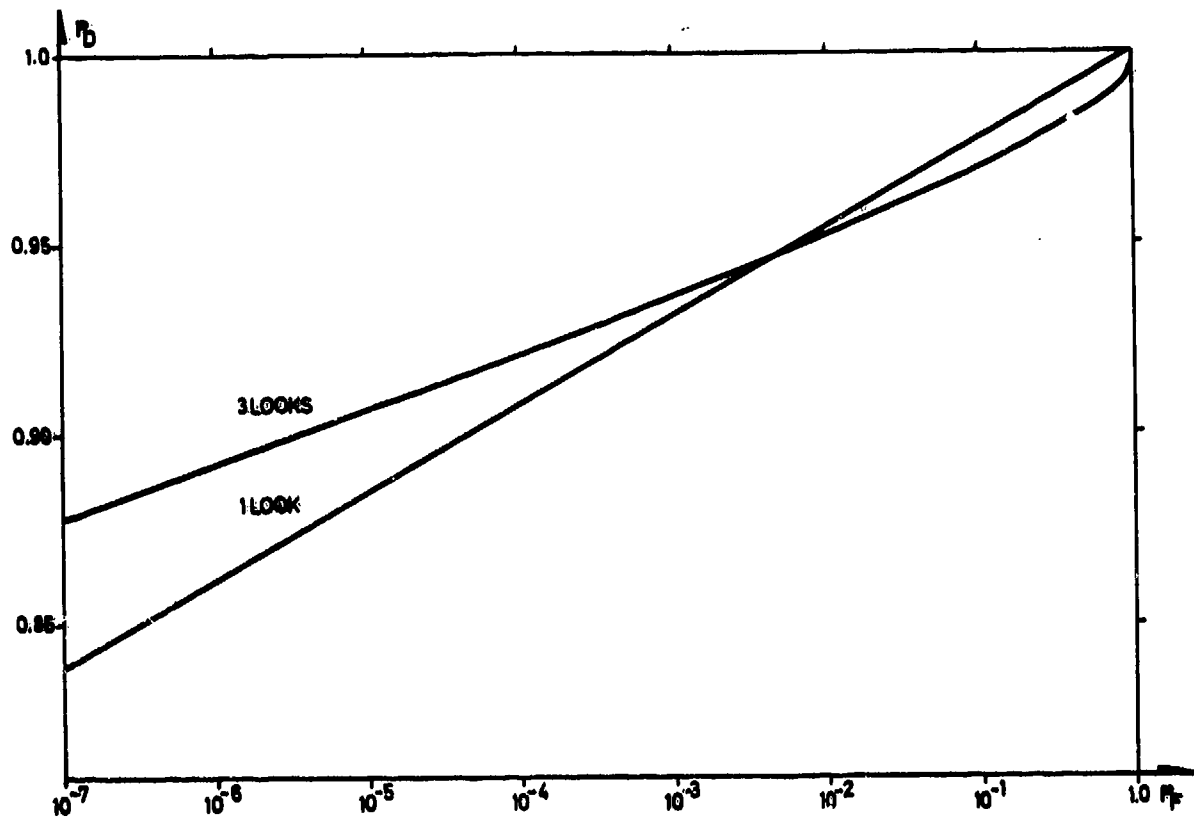
Figure 5.4 <u>Receiver operating characteristics for</u>
<u>an experimental case</u>

this may lead to a suppression of the target if it
becomes much smaller than the resolution cell. For a
SAR system like the one onboard SEASAT-1 it seems
unlikely that it should be advantageous to use so many
looks that this might occur.

6 CONCLUSION

As has been shown in the previous chapters, a satellite
borne synthetic aperture radar can very well be used
for maritime surveillance purposes. It is seen from
the examples of processed imagery that in many cases
ships can be seen clearly against the sea background.
An especially interesting phenomenon is the clear
visibility of the ship's wake, which probably appears
more clearly and lasts longer than it would in images
obtained in the optical frequency band.

The autofocusing procedure developed has been tried for
many different cases and works well for land areas.
Such a method is necessary when operational use of the
SAR imagery is intended, and may, depending upon the
quality of the estimation algorithms used for the
satellite orbit parameters, be adequate for maintaining
correct focus setting also for sea areas by updating
the estimates during passes over land.

When using the SEASAT-1 SAR system to evaluate the
usefulness of a satellite borne SAR system for mari-
time surveillance, it should be remembered that this
system was not designed for such a purpose. Some of
the design criteria were in fact the opposite of what
would be chosen for surveillance purposes. The
depression angle of 70° was for example, among other
reasons, chosen because this gives a rather high
backscatter coeffisient for the sea. When looking
for ships this results in a high sea clutter level
which makes the target detection more difficult. A
somewhat smaller depression angle would result in a
lower sea clutter level.

The main problem when using a satellite borne SAR
system for maritime surveillance, and digital proces-
sing of images, is the processing time. To be of any

operational value, the images would have to be processed within a few hours after the satellite had passed the area. The average processing rate would also have to be equal to the data acquisition rate. If the data rate is measured in km^2/sec, the acquisition rate for SEASAT-1 was approximately 700 km^2/sec. The images shown here are processed with a general purpose computer and with a rate of approximately 60 km^2/hour = 0.017 km^2/sec. If the average acquisition rate for an operational system should be of the order of 10 km^2/sec, this would require an increase in processing speed with a factor 600.

The target detection algorithm developed in chapter 5 will require processing to obtain empirical values for coherence times for typical targets. This has not yet been done, but a single example is given which illustrates the effect of changing the coherent integration time.

DOPPLER CENTROID ESTIMATION

The doppler centroid of the azimuth frequency spectrum
is estimated directly from a block of rawdata. The
real samples are converted to complex samples by
demodulating the range vectors so that the lowest
sideband is centered around 0 frequency, and then
lowpass filtering each range vector to reduce the
sampling frequency with a factor 2. Each azimuth
vector is then Fourier transformed, the spectrum is
averaged over 100 azimuth vectors, each of length 512
complex samples, and the doppler centroid is estimated
from the phase of the first harmonic of the frequency
spectrum.

Rawdata block with real samples

$$a(i,j), \quad i = 0,208, \quad j = 0,511, \quad <a(i,j)> = 0$$

i is range index and j is azimuth index. The lowest
sideband in range is centered at 11.38 MHz, which is
the real sampling frequency divided by four. Demodu-
lation gives

$$b(i,j) = a(i,j) \cdot \exp\{-j\tfrac{\pi}{2} \cdot i\}, \quad i = 0,208, \quad j = 0,511$$

Lowpass filtering with a truncated interpolation
filter gives the rawdata matrix on complex form

$$c(i,j) = \sum_{k=o}^{10} b(2i+k,j) \cdot \frac{\sin[(k-5)\tfrac{\pi}{2}]}{(k-5)\tfrac{\pi}{2}}, \quad i = 0,99, \quad j = 0,511$$

Fourier transformation in azimuth

$$H_i(k) = \sum_{j=o}^{511} c(i,j) \cdot \exp\{-j\tfrac{\pi}{256}k \cdot j\}, \quad k = 0,511, \quad i = 0,99$$

Averaged frequency spectrum

$$W(k) = \frac{1}{100} \sum_{i=0}^{99} |E_i(k)| \quad , \quad k = 0,511$$

First harmonic of $W(k)$ is

$$d = \sum_{k=0}^{511} W(k) \cdot \exp\{-j\frac{\pi}{256}k\} = r_d \cdot \exp\{-j\phi_d\}, \quad 0 \leq \phi < 2\pi$$

The doppler centroid estimate $\hat{f}_d$ is then

$$\hat{f}_d = \frac{\phi_d}{2\pi} \cdot PRF$$

PRF is the pulse repetition frequency of the radar. Through use of this estimation algorithm it seems that an accuracy of better than 100 Hz is obtained with PRF = 1647 Hz.

References

(1) Skolnik M I (1962): "Introduction to radar systems", McGraw-Hill, Inc.

(2) Tomiyasu K (1978): "Tutorial review of synthetic-aperture radar (SAR) with applications to imaging of the ocean surface", Proceedings of the IEEE, Vol 66.

(3) Brown W M, Porcello L J (1969): "An introduction to synthetic aperture radar", IEEE Spectrum, No 9.

(4) Jordan R L (1980): "The SEASAT-A synthetic aperture radar system", IEEE Journal of Oceanic Engineering, Vol OE-5, No 2.

(5) Thomas J B (1969): "An introduction to statistical communication theory", John Wiley and Sons, Inc.

(6) Kondinelli L A, Zeoli G W (1962): "Evaluation of the effect of random tropospheric propagation phase errors on synthetic array performance", Eighth Annual Radar Symposium Record, University of Michigan.

(7) Greene C A, Moller R T (1962): "The effect of normally distributed random phase errors on synthetic array gain patterns", IRE Transactions Military Electronics, Vol MIL-6, No 2.

(8) Goodman J W (1968): "Introduction to Fourier optics", McGraw-Hill.

(9) Goodman J W (1976): "Some fundamental properties of speckle", Journal of Optical Society of America, Vol 66, No 11.

(10) Cutrona L J, Leith E N, Porcello L J, Vivian W E (1966): "On the application of coherent optical processing techniques to synthetic aperture radar", Proceedings of the IEEE, Vol 54, No 8.

(11) Leith E N (1968): "Optical processing techniques for simultaneous pulse compression and beam sharpening", IEEE Transactions on Aerospace and Electronic Systems, Vol AES-4, No 6.

(12) Harger R O (1970): "Synthetic Aperture Radar Systems", Academic Press, Inc.

(13) Eklundh J O (1972): "A fast computer method for matrix transposing", IEEE Trans C-21.

(14) Rabiner L R, Gold B (1975):   "Theory and
     application of digital signal processing",
     Prentice-Hall, Inc.

(15) Brigham E O (1974):   "The Fast Fourier Transform",
     Prentice-Hall, Inc.

(16) Herland E A: Report in preparation.

(17) van Trees H L (1968):   "Detection, Estimation and
     Modulation Theory", Part I, John Wiley & Sons, Inc.

(18) Wainstein L A, Zubakov V D (1962):   "Extraction
     of signals from noise", Prentice-Hall.